

# **Fabrication of VO<sub>2</sub> (B) Thin Films by Pulsed DC Reactive Magnetron Sputtering and Characterization at Low and High Temperatures**

By

Juan José Pastrana González

A thesis submitted in partial fulfilment of the requirements for the degree of

MASTER OF SCIENCE  
In  
PHYSICS

UNIVERSITY OF PUERTO RICO  
MAYAGUEZ CAMPUS  
2017

Approved by:

\_\_\_\_\_  
Felix E. Fernández, Ph.D.  
President, Graduate Committee

\_\_\_\_\_  
Date

\_\_\_\_\_  
Jun-Qiang Lu, Ph. D.  
Member, Graduate Committee

\_\_\_\_\_  
Date

\_\_\_\_\_  
Pablo J. Marrero, Ph. D.  
Member, Graduate Committee

\_\_\_\_\_  
Date

\_\_\_\_\_  
Ricky Valentín, Ph. D.  
Representative of Graduate Studies

\_\_\_\_\_  
Date

\_\_\_\_\_  
Rafael A. Ramos, Ph. D  
Chairperson of the Department

\_\_\_\_\_  
Date

To Félix Fernández and Alfredo Moreu

*Your encouragement and advices has led me to places I never thought I would go. Your humility, tenacity, leadership, diligence and patience are my example to follow. The knowledge you have imparted upon me is an invaluable treasure...*

*The words "Thank you" are insufficient in their ability to convey the level of gratitude I have. I will always be in your debt...*

# Contents

<b>Declaration.....</b>	<b>vii</b>
<b>Acknowledgements .....</b>	<b>viii</b>
<b>Abstract.....</b>	<b>x</b>
<b>Resumen.....</b>	<b>xii</b>
<b>Chapter 1 Introduction.....</b>	<b>1</b>
1.1 Research Interest.....	1
1.2 Structures .....	2
1.2.1 VO <sub>2</sub> .....	2
1.2.2 V <sub>2</sub> O <sub>3</sub> .....	4
<b>Chapter 2 Previous Work.....</b>	<b>6</b>
2.1 Vanadium Oxides.....	6
2.1.1 VO <sub>2</sub> (M <sub>1</sub> ).....	6
2.1.2 VO <sub>2</sub> (B).....	11
<b>Chapter 3 Sputtering Technique .....</b>	<b>15</b>
3.1 Magnetron Sputtering .....	16
3.2 Reactive Sputtering.....	18
3.3 Pulsed DC Magnetron Reactive Sputtering .....	18
3.4 Instabilities in Reactive Sputtering .....	20
3.4.1 Hysteresis.....	20
3.4.2 Arcing .....	27
3.4.3 Disappearing Anode .....	27
3.5 Consequences of Target Erosion in Reactive Sputtering.....	28
<b>Chapter 4 Experimental Procedures.....</b>	<b>30</b>
4.1 Substrates .....	30
4.2 Cryogenic Vacuum Pump .....	30
4.2.1 Regeneration .....	31
4.3 Deposition Chamber .....	32
4.4 Ceramic Heater .....	34
4.5 Argon and Oxygen Atmosphere Pre-Sputtering .....	35
4.6 Characterization Techniques.....	36
4.6.1 X-ray Diffraction .....	36
4.6.2 Atomic Force Microscope.....	38

4.6.3	Electrical Measurements – Resistance and Resistivity .....	38
<b>Chapter 5</b>	<b>Results and Discussion.....</b>	<b>42</b>
5.1	X-ray Diffraction (XRD) Analysis .....	42
5.2	Electrical Characterization.....	49
5.3	Atomic Force Microscope (AFM) Analysis .....	57
<b>Chapter 6</b>	<b>Conclusion .....</b>	<b>60</b>
<b>References.....</b>		<b>63</b>

## List of Figures

**Figure 1.1** (a) Projection of VO<sub>2</sub> (R) along [010] in which vanadium atoms build chains parallel to c axis. (b) Projection of the same structure along [001] plane. Octahedron planes are z = 0 (white triangles) and z = ½ (grey triangles). Taken from [8]. Image created with VNL [9].....3

**Figure 1.2** (a) Projection along [010]. (b) Projection along [100] showing the ex-c axis of the rutile cell. Plane separation is in terms of x. Taken from [8]. Image created with VNL [9].....4

**Figure 1.3** Projection of the V<sub>2</sub>O<sub>3</sub> structure on a plane perpendicular to the  $\bar{1}\bar{1}0$  axis. Taken from [8]. Image created with VNL [9].....4

**Figure 1.4** This body-centered cell was chosen to describe the structure of the monoclinic phase of V<sub>2</sub>O<sub>3</sub> because it appears to be the correct conventional monoclinic cell. Atoms position taken from [12]. Image created with VNL [9].....5

**Figure 2.1** Conductivity of sputtered VO<sub>2</sub> thin film over randomly oriented sapphire substrate. Taken from [17].....7

**Figure 2.2** Resistivity curve from the 400 °C deposited sample. A hysteresis width was about 2 degrees while transition width was 10 degrees. Taken from [1].....9

**Figure 2.3** (a) As grain size increases, residual stress increases. At approximately 115 nm, residual stress begins to decrease. (b) Large hysteresis forms under large residual stress. Both taken from [19].....10

**Figure 2.4** Microcantilever’s curvature and stress as a function of temperature. As the transition occurs, film stress increases to approximately 1 GPa. Taken from [20].....10

<b>Figure 2.5</b> X-ray patterns of VO <sub>2</sub> (B) under 440 MPa at room temperature. Time varies as (a) 0, (b) 0.3, (c) 2, (d) 5 and (e) 20 hours. Open and closed circles are VO <sub>2</sub> (B) and VO <sub>2</sub> (A) respectively. Taken from [24].	12
<b>Figure 2.6</b> (a) VO <sub>2</sub> (B) XRD patterns at 300, 240, 200 and 50 K. Peaks of HTP and LTP are indexed. (b) Change in magnetic susceptibility as a function of temperature shows the new phase transition of VO <sub>2</sub> (B) at low temperatures. Both taken from [25].	13
<b>Figure 2.7</b> (a) Micrograph of VO <sub>2</sub> (B) and (b) micrograph of annealed VO <sub>2</sub> (B) which resulted in VO <sub>2</sub> (M). Both taken from [28].	14
<b>Figure 3.1</b> Electric and magnetic field directions in the right side of the magnetron cathode.	17
<b>Figure 3.2</b> Typical profile for a magnetron cathode. Taken from [32].	17
<b>Figure 3.3</b> Representation of a periodic waveform of target voltage for a pulsed DC for a bipolar pulse mode. Taken from [34].	20
<b>Figure 3.4</b> Instability in the system happens when an increased in pressure results from a decrease in reactive gas consumption. Based on diagram from [35].	21
<b>Figure 3.5</b> Poisoning of the vanadium pentoxide target.	23
<b>Figure 3.6</b> Voltage as a function of oxygen flow for 6.2 mTorr film deposition.	24
<b>Figure 3.7</b> Voltage as a function of oxygen flow for 20.2 mTorr working pressure film deposition.	25
<b>Figure 3.8</b> Voltage as a function of oxygen flow for vanadium target. Increasing the argon flow prevents hysteresis and increases the stable region.	26
<b>Figure 3.9</b> An increase in power results in a lengthening of the "metallic" region.	26
<b>Figure 3.10</b> Voltage as a function of oxygen flow for the target at 0.75 mm thickness and at a larger unknown thickness.	29
<b>Figure 4.1</b> Diagram and sections of the cryopump. Taken from [46].	31
<b>Figure 4.2</b> Residual gas analysis from the RGA shows base pressure is mostly composed of air and water vapor. Background pressure is $5.7 \times 10^{-8}$ Torr in this case, which was measured after 15 minutes of cryopumping the vacuum chamber.	33
<b>Figure 4.3</b> Result of the calibration between the controller and substrate's surface temperature.	35
<b>Figure 4.4</b> Bragg's X-ray Reflection.	37
<b>Figure 4.5</b> Resistivity measurement configuration for the samples.	39

<b>Figure 4.6</b> Diagram of the eight van der Pauw measurements. Arrow represents the direction of the current. Taken from [54].	41
<b>Figure 5.1</b> X-Ray diffraction 2-Theta patterns for samples J128 and J130.	43
<b>Figure 5.2</b> X-Ray diffraction patterns for samples grown at different temperatures, with 12.5 sccm O <sub>2</sub> flow.	44
<b>Figure 5.3</b> X-ray diffraction pattern for VO <sub>2</sub> grown over STO substrate at two different temperatures.	45
<b>Figure 5.4</b> X-ray diffraction for samples grown at different temperatures under 11.5 sccm oxygen flow rate, in contrast with previous samples.	46
<b>Figure 5.5</b> (a) VO <sub>2</sub> (B) films deposited over SiO <sub>2</sub> substrates and (b) STO substrates. Compared with powder X-ray diffractions, peaks of VO <sub>2</sub> (B) films are shifted to higher angles.	49
<b>Figure 5.6</b> Arrhenius-type plot of the electrical conductivity for sample J128; inset: resistivity as a function of temperature. No hysteresis is observed from 300 to 120 K.	50
<b>Figure 5.7</b> Arrhenius behaviour is observed with ln( $\sigma$ ) as a function of 1/T for T $\gtrsim$ 150 K.	51
<b>Figure 5.8</b> ln(Resistivity) as a function of temperature for samples (a) J127 and (b) J130.	52
<b>Figure 5.9</b> ln(Resistivity) as a function of temperature displays a change of slope for (a)-(b) sample J128 and (c)-(d) sample J130.	53
<b>Figure 5.10</b> ln(Resistivity) as a function of temperature displays a change of slope to higher temperatures for (a)-(b) sample J162, (c)-(d) sample J163 and (e)-(f) sample J165. Higher temperature shift is attributed to deviation from stoichiometry for VO <sub>2</sub> (M <sub>1</sub> ).	54
<b>Figure 5.11</b> Resistivity vs. temperature for VO <sub>2</sub> (B) thin films grown over STO substrate. Characteristic hysteresis behaviour of the M <sub>1</sub> phase undergoing transition is observed in sample (a) J129 and (b) J132.	55
<b>Figure 5.12</b> (a) Linear fit for 250-300 K temperature range and (b) linear fit for 300-350 K temperature range for sample J128.	56
<b>Figure 5.13</b> (a) AFM image for sample J162. (b) Surface height distribution is ~38 nm. (c) Average lateral grain size is ~121 nm.	58
<b>Figure 5.14</b> (a) AFM image for sample J165. (b) Surface height distribution is ~34 nm. (c) Average lateral grain size is ~158 nm.	59

## **Declaration**

I hereby declare that my thesis is entirely the result of my own work. I have faithfully and accurately cited all my sources such as books, journals, handouts and unpublished manuscripts, as well as any other media such as Internet, letters or significant personal communication. In addition, the content of this thesis has not been submitted in whole or in part for consideration for any other degree or qualification in this or any other University.

Juan José Pastrana González

2017

## Acknowledgements

This thesis is based upon work supported by the U.S Army Research Laboratory and the U.S Army Research Office under contract number W911NF-15-1-0448.

I'll start by thanking my mother and father. They have sacrificed their lives for my sister and myself, providing unconditional love and care. I would not have made it this far without them.

To Dr. Jun-Qiang Lu for giving me the chance to learn computational physics. He provided me with opportunities to develop in the personal and academic matter. Thank you very much.

Dr. Pablo J. Marrero, thank you for your teachings and insight. Always available for any question I had.

Dr. José R. López, thank you for giving me the opportunity to learn from you as a professor and to be part of the AFAMaC team. For showing me that education must be delivered to those who may not have the resources to obtain it.

To Denisse Perdómo and Nicole Irizarry, thank you for always caring and for being ready to help anytime.

To Jessica Pérez and Lizbeth Rodríguez, for giving me the opportunity to become a friend. For your understanding and for the help you provided me since the beginning. Thank you for the beautiful experiences.

My thanks to Waleska Cruz for lending the tools and instruments when I needed them ASAP. In addition, the coffee you made helped me on the long working days.

I would like to thank Juan A. Santiago Santos for helping me getting started with the sputtering machine. I appreciated the time you took to answer my questions.

My sincere thanks to Dr. Sergiy Lysenko for giving me the chance to work with the Advance Materials Group. To Dr. Armando Rúa for helping me characterize my samples with the X-ray machine. In addition, he kindly gave me the data of one of his samples for comparison. Thank you.

My thanks to Ramón D. Díaz Martínez for teaching and helping me with the LabVIEW program he created.

To the family of “El Colegial”, specially to Luis Acosta. For giving me work when I needed it the most, I will always be thankful.

To my friends José Figueroa, Giovanni Franco, Segundo Rojas, Moises Gallozo, Angel Perez, Carlos Llaurador, David Perez, Angela Ferrá, Angel Figueroa and Alberto Lugo. Thank you for your support and for making these years a wonderful journey.

To my advisor Dr. Felix Fernández. For having me as an undergraduate and as a graduate student. For undertaking the challenge of guiding me. For your patience and motivation. Most of all, for being a role model to follow. I could have not asked for a better mentor. Thank you so much.

To mechanical engineer Alfredo Moreu. Your expertise were an indispensable tool for this work. Thank you for all your practical, academic and personal teachings. Thank you for being a counselor, a mentor and a great friend.

## Abstract

For this work, VO<sub>2</sub> (B) thin films were fabricated using pulsed DC magnetron reactive sputtering. The technique belongs to the ionic sputtering methods which allows high deposition rates, high-purity films, excellent uniformity and high adhesion of films. Reactive sputtering suffers from one drawback called target "poisoning", which causes a hysteretic control problem and results in instabilities in the fabrication process. For the purpose of having a better control in the film's fabrication, measurements of cathode voltage in the sputtering gun as a function of oxygen flow were performed at different gun power settings. Based on the results, the parameters which presented the best conditions for film growth were as follows: Argon working pressure of 5 - 6.2 mTorr, argon flow of 100 standard cubic centimeters per minute (sccm), 11.5 - 12.5 sccm oxygen flow and gun power of 200 Watts. Thin films were deposited over fused silica glass (SiO<sub>2</sub>) at 350 °C and 375 °C. X-ray characterization showed VO<sub>2</sub> (B) films grown in this manner present strong preferential crystallization orientation with (001) planes parallel to the substrate surface. In addition, peaks are shifted to higher angles, evidencing that the films are in tensile stress. Electrical measurements were done through heating-cooling cycles from 400 to 120 K. Resistivity measurements showed a drop of 6 orders of magnitude while cooling from 300 to 120 K. Graphing conductivity as a function of temperature showed no hysteresis, in agreement with recent reports. The linear behaviour was described by an Arrhenius plot in which activation energy is 137 meV. A Temperature Coefficient of Resistance (TCR) of -3.6% and -1.7% K<sup>-1</sup> for cooling and heating cycles was calculated, respectively. Also, a detailed analysis for the heating cycle (300 - 400 K) of the samples was done. High temperature resistivity measurements for VO<sub>2</sub> (B) films prepared at 350 °C showed a change of slope at ~68 °C indicating the admixture of VO<sub>2</sub> (M<sub>1</sub>). On the other hand, samples prepared at 375 °C showed a change of slope at ~79 °C, representing a small

concentration of VO<sub>2</sub> (M<sub>1</sub>) with higher oxidation composition. Finally, two samples were analysed by atomic force microscopy (AFM). Surface roughness (RMS) values obtained were 10 and 13 nm respectively. The average lateral grain size was calculated using Heyn's technique, obtaining values of 121 nm for one sample and 158 nm for the other. The grain size results in numerous imperfections, having an impact on the electrical properties of VO<sub>2</sub> (B): it is possible that larger grain sizes will result in higher conductivity samples. This study may provide the possibility to fabricate VO<sub>2</sub> (B) thin films that are relevant for both, infrared sensing applications and lithium-ion batteries cathode material.

## Resumen

Para este trabajo, las películas delgadas de VO<sub>2</sub> (B) se fabricaron utilizando bombardeo reactivo con magnetrón DC pulsado. La técnica pertenece a los métodos de pulverización iónica (sputtering) que permite altas tasas de deposición, películas de alta pureza, excelente uniformidad y alta adhesión de películas. El sputtering sufre de un inconveniente llamado oxidación del blanco, causando un problema de control de la histéresis y produciendo inestabilidades en el proceso de fabricación. Con el fin de tener un mejor control en la fabricación de las películas, la medición de voltaje del cátodo del cañón como una función del flujo de oxígeno se realizaron a diferentes configuraciones de potencia del cañón. En base a los resultados, los parámetros que presentaron las mejores condiciones para el crecimiento de película fueron los siguientes: presión de trabajo de argón de 5 - 6.2 mTorr, flujo de argón de 100 centímetros cúbicos estándar por minuto (sccm), flujo de oxígeno de 11.5 - 12.5 sccm y potencia de cañón de 200 vatios. Las películas delgadas se depositaron sobre sílicio fundido (SiO<sub>2</sub>) a 350 °C y 375 °C. La caracterización por rayos X mostró que las películas de VO<sub>2</sub> (B) crecidas de esta manera presentan una fuerte orientación de cristalización con planos (001) paralelos a la superficie del sustrato. Además, los picos fueron desplazados a ángulos de mayor grado, lo que demuestra que las películas están en tensión. Las mediciones eléctricas se realizaron a través de ciclos de calentamiento-enfriamiento de 400 a 120 K. Las mediciones de resistividad mostraron una caída de 6 órdenes de magnitud al enfriar de 300 a 120 K. Se observó una caída en la conductividad sin histéresis de acuerdo con informes recientes. El comportamiento lineal fue descrito por un diagrama de Arrhenius en el cual la energía de activación es 137 meV. Se calculó un coeficiente de resistencia de temperatura (TCR) de -3.6% y -1.7% K<sup>-1</sup> para los ciclos de enfriamiento y calentamiento, respectivamente. Por otra parte, se realizó un análisis detallado del ciclo de calentamiento (300 - 400 K) de las muestras. Las mediciones de resistividad a alta temperatura para películas de VO<sub>2</sub> (B) preparadas a 350 °C

mostraron un cambio de pendiente a  $\sim 68$  °C que indica la mezcla de VO<sub>2</sub> (M<sub>1</sub>). Por otro lado, las muestras preparadas a 375 °C mostraron un cambio de pendiente a  $\sim 79$  °C, lo que representa una pequeña concentración de VO<sub>2</sub> (M<sub>1</sub>) con mayor composición de oxígeno. Finalmente, se analizaron dos muestras mediante microscopía de fuerza atómica (AFM). Los valores de rugosidad superficial (RMS) obtenidos fueron de 10 y 13 nm respectivamente. El tamaño medio del grano lateral se calculó utilizando la técnica de Heyn, obteniendo valores de 121-nm para una muestra y 158 nm para la otra. La estructura de los granos da como resultado numerosas imperfecciones, teniendo un impacto en las propiedades eléctricas del VO<sub>2</sub> (B). Es posible que los mayores tamaños de grano den como resultado muestras con conductividad más altas. Este estudio puede proporcionar la posibilidad de fabricar películas delgadas de VO<sub>2</sub> (B) que son relevantes tanto para aplicaciones de detección de infrarrojos como para baterías con cátodos de litio.

# Chapter 1 Introduction

## 1.1 Research Interest

Oxide materials that undergo reversible transitions between metallic and insulating states have been of great interest for both theoretical and practical reasons. Their unique physical properties, along with their phase transitions at different temperatures, offer a wide range of applications in the fields of high speed electronics, memory devices, electro-chromic and thermo-chromic applications, field emission displays, cathode material in batteries, etc. Among these strongly correlated materials, vanadium oxides can adopt a wide range of V:O ratios that result in different structural motifs which determine their physical properties. The most studied of these materials is vanadium dioxide ( $\text{VO}_2$ ), but several other vanadium oxides have been studied to varying degrees.

Vanadium dioxide is well known for its metal-to-insulator transition (MIT) at 340 K.<sup>1</sup> This transition results from a structural change from a tetragonal rutile-type (R) to monoclinic ( $M_1$ ) lattice.<sup>1-2</sup> The transformation is accompanied by substantial changes in the material's electrical properties by several orders of magnitude and in optical properties as well. In bulk crystals, the resistivity changes in the order of  $10^5 \Omega \cdot \text{cm}^{-1}$   $\text{VO}_2$  thin films, on the other hand, have lower changes in the resistivity values. Optical properties are affected in the near infrared region. In addition, vanadium dioxide exhibits a number of polymorphic forms besides the  $M_1$  and R phases. These include those labelled as  $M_2$ , A and B. Vanadium sesquioxide ( $\text{V}_2\text{O}_3$ ) also shows a much-studied MIT. At the Néel Temperature (180 K),  $\text{V}_2\text{O}_3$  crystals present an abrupt drop of 6 orders of magnitude in resistivity.<sup>3</sup> In contrast, thin films only present a change by 3-5 orders, although, this is highly dependent upon possible stresses between the film and the substrate.<sup>4</sup>

Vanadium is a transition metal that can show a rich phase diagram of diverse oxidation states (+2, +3, +4 and +5). In the V valence range from +3 to +4 there are seven discrete phases

that are described by the homologous series  $V_nO_{2n-1}$ , with  $n$  from 3 to 9, called the Magnéli series. It is bordered in the phase diagram by  $V_2O_3$  and  $VO_2$ , which are not members of the series.<sup>5</sup> Each of the phases present different structures and properties. Only one vanadium oxide in the Magnéli series does not have a metal-insulator phase transition.

Various techniques are used to deposit vanadium oxide thin films. Some of them are Pulsed Laser Deposition (PLD), Sol-Gel synthesis, evaporation, Chemical Vapor Deposition (CVD) and sputtering. PLD is likely the most popular to work with these oxides. Following up is reactive sputtering, which was used for the present work. In general, each technique presents advantages and limitations. While PLD has been shown to be capable of producing excellent quality films, it is not a very suitable technique for large-scale applications, unlike sputtering.

Many of these oxides are deposited at high temperatures, and this growth temperature is an important factor in the resulting phase of the as-deposited film.<sup>6</sup> Once the temperature starts to decrease, after deposition, stress can appear due to differences in the coefficient of thermal expansion of the film and the substrate. This resulting stress can affect intrinsic properties of the film and have an impact in their performance. Also, and more importantly, deviations from exact stoichiometry can have a very significant effect on properties. The purpose of this research is to seek optimal growth conditions in which vanadium oxide thin films with certain particular compositions can be grown by reactive sputtering and study the electrical properties of the resulting films.

## 1.2 Structures

### 1.2.1 $VO_2$

Vanadium dioxide shows a rich phase diagram with polymorphs like  $VO_2$  ( $M_1$ ),  $VO_2$  ( $R$ ),  $VO_2$  ( $A$ ),  $VO_2$  ( $B$ ),  $VO_2$  ( $D$ ),  $VO_2$  ( $BBC$ ) and  $VO_2$  ( $N$ ). Polymorphs  $D$ ,  $BCC$  and  $N$  were recently discovered, and their study is just beginning.<sup>7</sup> Generally speaking, the structures of these polymorphs are based on an oxygen *bcc* lattice with vanadium being in the octahedral sites.

Depending on the orientation of the fourfold axis of the oxygen octahedral different polymorphs will result.

The most stable structure is VO<sub>2</sub>(R). It is stable from 341 K to 1813 K with tetragonal cell parameters  $a = b = 4.55 \text{ \AA}$ ,  $c = 2.88 \text{ \AA}$ ,  $Z = 2$ ; the space group is  $P4_2/mmm$  (S.G. #136).<sup>8</sup> This structure is rutile type. Observing figure 1.1, all V atoms are equally spaced along linear chains of VO<sub>6</sub> octahedral, having a distance between them of 2.86 Å.

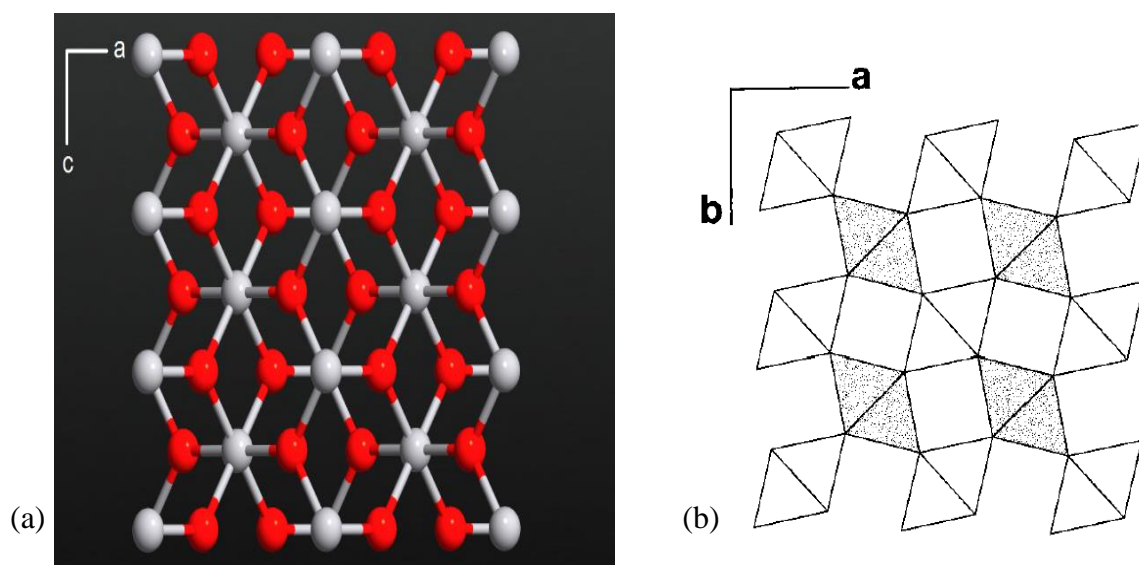


**Figure 1.1:** (a) Projection of VO<sub>2</sub> (R) along [010] in which vanadium atoms build chains parallel to **c** axis. (b) Projection of the same structure along [001] plane. Octahedron planes are  $z = 0$  (white triangles) and  $z = 1/2$  (grey triangles). Taken from [8]. Image created with VNL [9].

When temperature is lower than 341 K, the VO<sub>2</sub>(R) structure changes from to a monoclinic (M<sub>1</sub>) phase. Looking at figure 1.2, the V-V bond distance, which was 2.86 Å, is observed to become in alternating sequence, 2.65 Å and 3.12 Å. This is due to the pairing and tilting of VO<sub>6</sub> octahedra with respect to the rutile **c** axis. The cell parameters of the VO<sub>2</sub> (M<sub>1</sub>) phase are  $a = 5.75 \text{ \AA}$ ,  $b = 5.42 \text{ \AA}$ ,  $c = 5.38 \text{ \AA}$ ,  $Z = 4$ ; the space group is  $P2_1/c$  (14).<sup>6</sup>

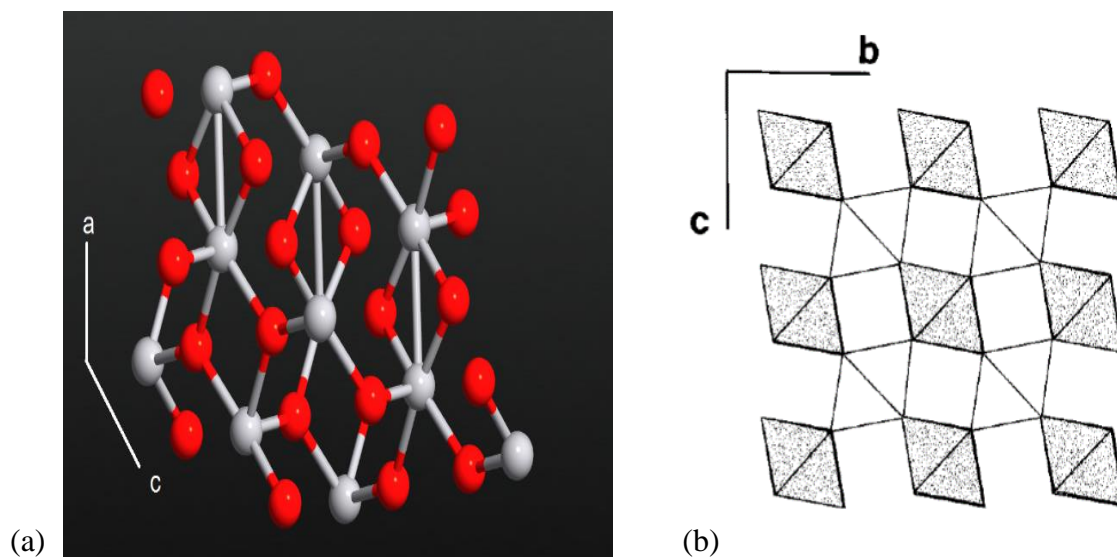


**Figure 1.2** (a) Projection along  $[010]$ . (b) Projection along  $[100]$  showing the  $ex-c$  axis of the rutile cell. Plane separation is in terms of  $x$ . Taken from [8]. Image created with VNL [9].

### 1.2.2 $V_2O_3$

Vanadium sesquioxide,  $V_2O_3$ , is also one of the most studied materials among the vanadium oxides. At room temperature,  $V_2O_3$  has metallic conduction and presents a corundum type structure with space group  $R\bar{3}c$ . For this space group, the hexagonal setting cell parameters are  $a = b = 4.925 \text{ \AA}$ ,  $c = 13.834 \text{ \AA}$ ;  $Z = 6$ .<sup>10</sup> The structure is paramagnetic and shows thermochromism behaviour in the infrared. At the visible spectrum, it retains its transparency.

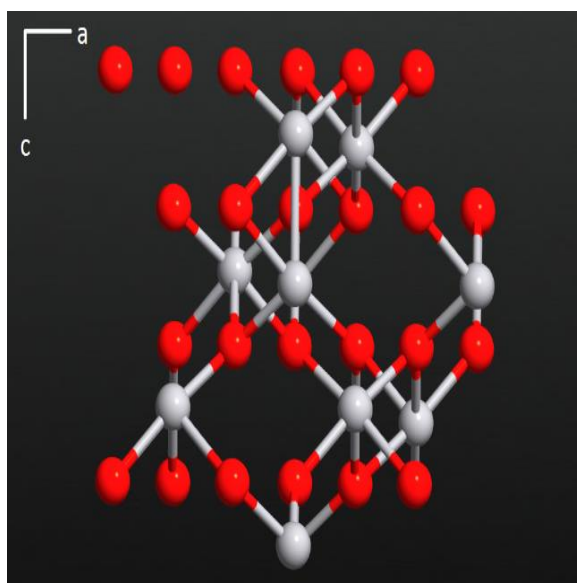


**Figure 1.3:** Projection of the  $V_2O_3$  structure on a plane perpendicular to the  $[\bar{1}10]$  axis. Taken from [8]. Image created with VNL [9].

Upon cooling, at 160 K,  $V_2O_3$  presents a phase transition from paramagnetic trigonal to an insulating-antiferromagnetic monoclinic structure  $C2/c$  ( $I2/a$ ). The symmetry change is associated with pairing of the vanadium ions along one of three basal-plane axes and a simultaneous tilting of the  $c$  axis.<sup>11</sup> The cell parameters are then  $a = 7.255 \text{ \AA}$ ,  $b = 5.002 \text{ \AA}$ ,  $c = 5.548 \text{ \AA}$ ,  $\beta = 96.75^\circ$ ,  $Z = 4$ .<sup>12-13</sup>

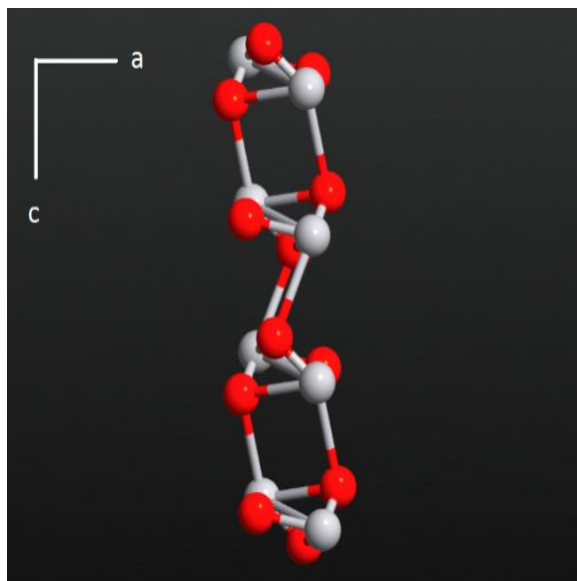


**Figure 1.4:** This body-centered cell was chosen to describe the structure of the monoclinic phase of  $V_2O_3$  because it appears to be the correct conventional monoclinic cell. Atoms position taken from [12]. Image created with VNL [9].

## Chapter 2 Previous Work

### 2.1 Vanadium Oxides

Some of the earliest works on phase transitions in vanadium oxides date back to 1942, when Foëx studied  $V_2O_3$  powders.<sup>14</sup> A phase transition was observed but not fully understood. Later, in 1958, F. J. Morin studied phase transitions in several oxides of the 3d transition metals.<sup>15</sup> Because no detailed determination of transport or band structure had been made for those oxides, he suggested an energy band scheme to examine various band structures. He concluded that a  $3d$  band exists in the oxides of vanadium. He also pointed out that  $V_2O_3$  shows a transition from metal-to-insulator (MIT) at the Néel temperature. In a second paper, Morin confirmed this transition with single crystals of VO,  $V_2O_3$  and  $VO_2$ .  $VO_2$  samples showed a conductivity change of two orders of magnitude. Transition temperature ranged from 335 – 350 K on heating and 340 – 325 K on cooling.<sup>3</sup> It is important to point out that his samples were 0.1 mm in size, which were too small for the four-point measurements. Thus, the absolute value of the conductivity presented was somewhat in doubt.

In the following section only some  $VO_2$  polymorphs will be discussed. Our interest is on thin films exhibiting phase transitions accompanied by changes in electrical properties, and contrasting them with electrical properties reported for powders and crystals. Although  $VO_2(R)$  and  $VO_2(M_1)$  have been studied for more than six decades, most relevant properties reported for thin films will be discussed. Furthermore,  $VO_2(B)$  in thin film form has been much less studied than  $VO_2(M_1)$  and little or no work has been previously reported for  $VO_2(B)$  deposited with the fabrication technique here presented, not to mention the electrical properties in a full heating-cooling cycle.

#### 2.1.1 $VO_2(M_1)$

Morin studied single crystals of  $VO_2$ , showing the first results for the transition in  $VO_2$ . He also presented a model to explain how the transition occurred.

The first VO<sub>2</sub> thin films produced by reactive sputtering were produced by Fuls *et al.* in 1967.<sup>16</sup> This was carried out with a standard DC sputtering apparatus. An argon pressure of 20 mTorr was used, with a small amount of oxygen. Sputtering rate was 35 Å/m which is lower than most transition metals sputtering rates. A pre-sputtering of 15 minutes was allowed for target stabilization. Randomly oriented sapphire substrates were heated at 400 °C during deposition and a 30 minutes post-deposition annealing was performed. Although the data was not presented in the paper, authors mention that X-ray diffraction confirmed the crystal structure at room temperature to be monoclinic VO<sub>2</sub>. As seen in figure 2.1, conductivity measurements were made in the temperature range from ambient to 150 °C. The reason for this upper limit was that the four-point indium contacts would melt at higher temperatures.

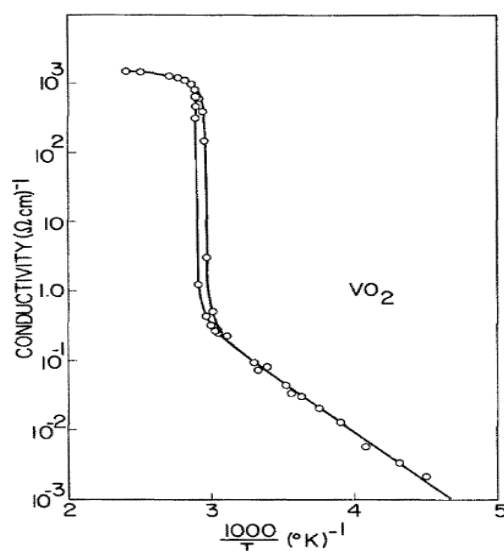


**Figure 2.1:** Conductivity of sputtered VO<sub>2</sub> thin film over randomly oriented sapphire substrate. Taken from [17].

The following year, Rozgonyi and Hensler used the same method and conditions as in the previous work to deposit VO<sub>2</sub> thin films.<sup>17</sup> They deposited over amorphous glass, glazed ceramic, single-crystal sapphire and rutile. Results showed that the magnitude of the transition for the films on glass and ceramic was less than for the films on rutile and sapphire by a factor of 40. Also, the transition on glass and ceramic substrates was spread out over a wider temperature range. Films over rutile had a 9 °C lower transition temperature than for other

substrates. These authors also found that for films deposited on amorphous glass or ceramic substrates, grains were small. In comparison, highly textured VO<sub>2</sub> was obtained over sapphire or rutile. Films over single crystal substrates also showed higher conductivity.

E.E Chain grew the first vanadium dioxide films deposited by reactive ion-beam sputtering method with a 5-inch diameter vanadium target.<sup>18</sup> The purpose was to study the influence of substrate temperature on the properties of the resulting films. With oxygen background pressure of  $3 \times 10^{-4}$  Torr, films were deposited over a range of 350-620 °C. Lower temperatures (350 – 435 °C) produced films with poorly defined grains while higher temperatures (585 - 620 °C) produced large, well-defined grains (1- 2µm in size). One film deposited at high temperature showed a decrease in electrical resistivity through the transition by a factor of 1500. These results suggest that an important factor to obtain large resistivity ratios in VO<sub>2</sub> is large grain size in the film.

VO<sub>2</sub> thin films were deposited by direct-current magnetron reactive sputtering by Kusano *et al.* in 1987.<sup>1</sup> A pure vanadium target was used to grow films over borosilicate glass plates. Infrared heating lamps were used to heat up the films. Argon pressure was held constant at 2 mTorr while partial pressure of oxygen was varied from 0 to 0.7 mTorr and temperatures from 300 to 500 °C. Film thickness were between 400 and 700 nm. They successfully deposited single-phase VO<sub>2</sub> films, although the presence of minority phases was not excluded. Higher resistivity films were obtained at 400 °C. As seen in figure 2.2, the sample grown at 400 °C displayed a hysteresis with a width of approximately 2 degrees and a transition range of ~9 degrees.

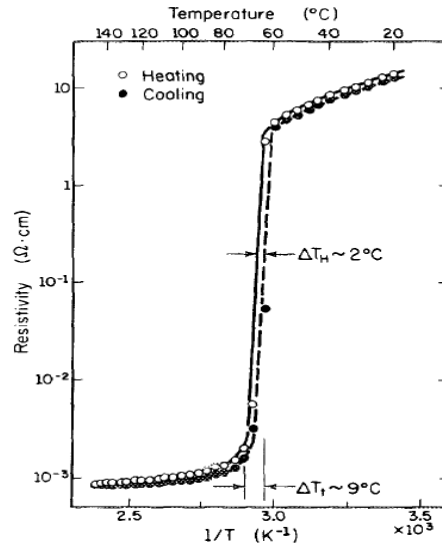


**Figure 2.2:** Resistivity curve from the 400 °C deposited sample. A hysteresis width was about 2 degrees while transition width was 10 degrees. Taken from [1].

The relationship between stresses and properties of VO<sub>2</sub> thin films has also been studied, as reported by Tsai and Chin.<sup>19</sup> Their films were deposited by RF-magnetron sputtering onto glass substrates. Pre-mixing of argon and oxygen gas was done in a small chamber at a positive pressure before being led into the vacuum chamber. Total working pressure was about 40 mTorr. They reported that residual stress increases in the film with increasing grain size, as seen in figure 2.3 (a). In addition, figure 2.3 (b) shows a relationship between the residual stress and the hysteresis width. Residual stress includes intrinsic and external stress. Intrinsic stress is associated with deposition process and microstructures. External stress is associated to the interaction between film and substrate. During the phase change of VO<sub>2</sub>, atoms move only locally which means there is no release of the residual stress. Upon heating, if the residual stress is large, the intrinsic stress should be larger to overcome the barrier of the phase change. Upon cooling, a large delay time of phase change is also required to make the film return to its original state of large residual stress. Therefore, these authors concluded that a large residual stress implies a large hysteresis width.

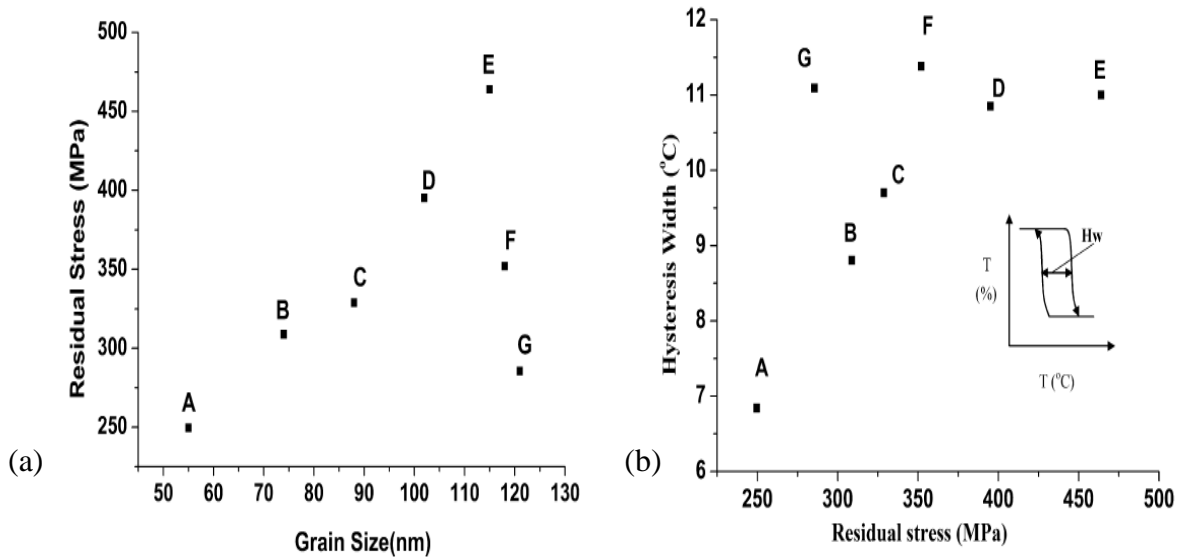


**Figure 2.3:** (a) As grain size increases, residual stress increases. At approximately 115 nm, residual stress begins to decrease. (b) Large hysteresis forms under large residual stress. Both taken from [19].

More recently, studies of stress on bending VO<sub>2</sub>-coated cantilevers have been made.<sup>20</sup> Films on microcantilevers showed an increase in film tension by bending towards the film side. The cantilever's tip displacement as a function of temperature was measured and the curvature was calculated. As seen in figure 2.4, film stress causing bending was approximately 1 GPa. Results showed that cantilevers or similar structures coated with VO<sub>2</sub> can be used as thermally driven transducers with very small dimensions.

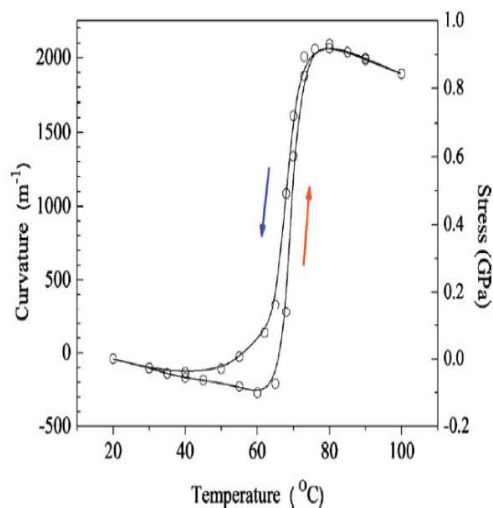


**Figure 2.4:** Microcantilever's curvature and stress as a function of temperature. As the transition occurs, film stress increases to approximately 1 GPa. Taken from [20].

### 2.1.2 VO<sub>2</sub> (B)

Discovery of this polymorph was reported by Théobald *et al.* in 1976.<sup>21</sup> Reduction of V<sub>2</sub>O<sub>5</sub> by several gases (hydrothermal synthesis) allowed the production of various vanadium oxides, one of them being VO<sub>2</sub> (B).

VO<sub>2</sub> (B) has a monoclinic structure with parameters  $a = 12.03 \text{ \AA}$ ,  $b = 3.693 \text{ \AA}$ ,  $c = 6.42 \text{ \AA}$  and  $\beta = 106.6^\circ$ . It belongs to the space group  $C \frac{2}{m}$ . The authors pointed out that the polymorph is derived from V<sub>2</sub>O<sub>5</sub> by crystallographic shear. Comparison between V<sub>6</sub>O<sub>13</sub> and VO<sub>2</sub> (B) structures were made and the authors conclude the polymorph belongs to the same series as V<sub>6</sub>O<sub>13</sub>. Further investigations were made but no uniform description of the structure relationship between VO<sub>2</sub> phases existed.<sup>22</sup>

Ten years later, Oka *et al.* found the first relationship between the phases of VO<sub>2</sub> (B) and VO<sub>2</sub> (A).<sup>23</sup> According to these authors, both structures consist of three-dimensional VO<sub>6</sub> octahedral frameworks arranged in sheets. These VO<sub>6</sub> sheets in both VO<sub>2</sub> (A) and VO<sub>2</sub> (B) are isostructural. The difference is the way these sheets are superimposed. The next year, the same authors prepared powder samples of monophasic VO<sub>2</sub> (B) and a mechanical stress of 440 MPa was applied to the samples followed by subsequent heat treatment and were compared with the non-stressed samples, as seen in figure 2.5.<sup>24</sup> They found a structural phase transition from VO<sub>2</sub> (B) to VO<sub>2</sub> (A). This transition corresponds to a change in structural units accomplished by the shift of oxygen vacancies along with rearrangements of vanadium atoms. The key feature of the transition is that it is induced mechanochemically although it is very slow.

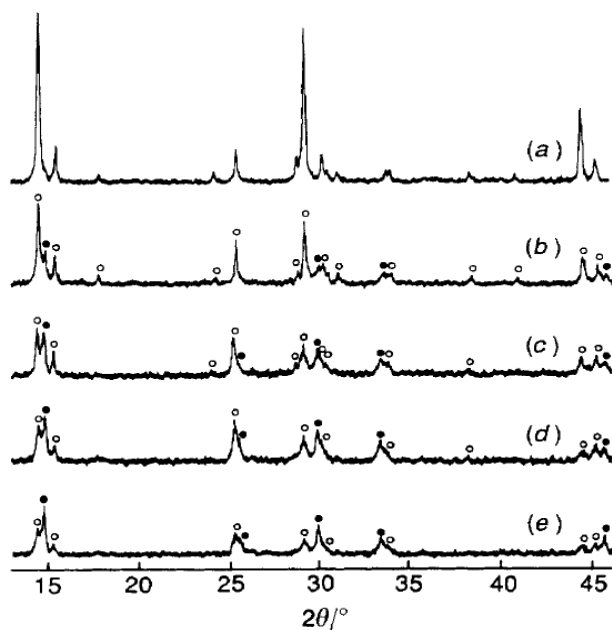


**Figure 2.5:** X-ray patterns of VO<sub>2</sub>(B) under 440 MPa at room temperature. Time varies as (a) 0, (b) 0.3, (c) 2, (d) 5 and (e) 20 hours. Open and closed circles are VO<sub>2</sub>(B) and VO<sub>2</sub>(A) respectively. Taken from [24].

Previously, it was demonstrated that under stress and subsequent annealing treatments, a structural transition from VO<sub>2</sub>(B) to VO<sub>2</sub>(A) was possible. This also demonstrated the relationship between these two polymorphs. Later, a new phase transition at low temperatures was found by Oka *et al.*<sup>25</sup> Magnetic properties and X-ray diffraction revealed a structural phase transition over the temperature range of 300 to 180 K, as seen in figure 2.6 (a)-(b). Both phases are monoclinic and were designated as high-temperature phase (HTP) and low-temperature phase (LTP) respectively. X-ray diffraction revealed a significant decrease in the V - V distance from 0.2867 to 0.2670 nm. Also, a decrease in magnetic susceptibility provides evidence for a V<sup>4+</sup>-V<sup>4+</sup> pairing for half of the V sites in the LTP. The LTP structure, according to these authors, is monoclinic ( $C \frac{2}{m}$ ) with parameters  $a = 1.2152 \text{ nm}$ ,  $b = 0.3799 \text{ nm}$ ,  $c = 0.6347$  and  $\beta = 107.58^\circ$ .



to 475 °C. The annealed samples showed a drop in resistivity at 68 °C, corresponding to the properties of VO<sub>2</sub> (M<sub>1</sub>)/VO<sub>2</sub>(R) phases. SEM images were taken from the (B) and (M<sub>1</sub>) phase. VO<sub>2</sub> (B) thin films deposited on S<sub>3</sub>N<sub>4</sub> substrate had a fine polycrystalline structure with grains uniformly spreading over the surface. Average grain height was 50 nm and diameter was between 100 and 250 nm. Compared to the (M), VO<sub>2</sub> (B) thin film is composed of scalelike crystallite and has a loose structure, as seen in figure 2.7 (a). In figure 2.7 (b), some cracking in the film is indicated.

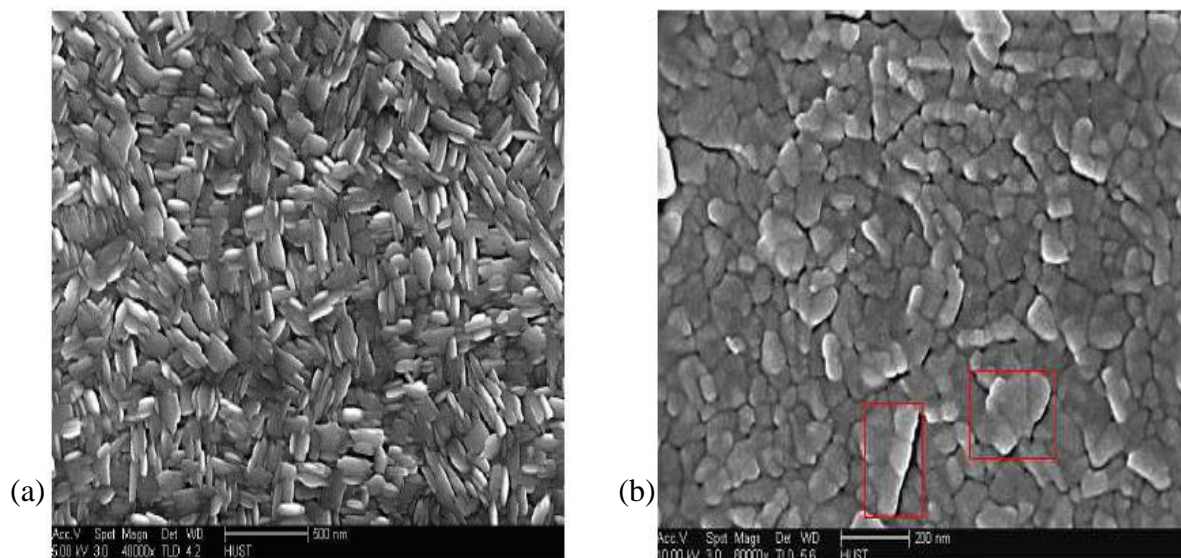


**Figure 2.7:** (a) Micrograph of VO<sub>2</sub> (B) and (b) micrograph of annealed VO<sub>2</sub> (B) which resulted in VO<sub>2</sub> (M). Both taken from [28].

VO<sub>2</sub> (B) thin film samples were grown by pulsed laser deposition (PLD) on different substrates by Rúa *et al.*<sup>29</sup> A total pressure of 70 mTorr was used with Ar/O<sub>2</sub> gas flows of 10 and 15 sccm respectively. The growth temperature to produce nearly pure VO<sub>2</sub> (B) ranged from 375 to 425 °C. XRD analyses showed strong (00*l*) reflection peaks. In addition, cooling-heating cycle conductivity measurements were done using a 4-point van de Pauw configuration. Over the cooling-heating cycle (from ambient to 120 K), conductivity changed by five orders of magnitude and no hysteresis was displayed, in contrast with results by Srivastava *et al.*<sup>30</sup> Surface morphology showed an average grain size of 50 and 90 nm. Compared to previous authors, grain size is much smaller.

## **Chapter 3    Sputtering Technique**

Several physical vapor deposition (PVD) methods exist for producing coatings in a vacuum environment. These can be separated in two groups: (a) involving thermal evaporation techniques and (b) involving ionic sputtering methods. Pulsed DC Magnetron Sputtering belongs to the latter group. It is a very powerful technique that presents many advantages. It allows high deposition rates, high-purity films, ability to coat heat-sensitive substrates, ease of sputtering any metal, alloy or compound, excellent uniformity and high adhesion of films.<sup>31</sup>

A target (or cathode) plate is bombarded by energetic ions generated in a glow discharge plasma, situated in front of the target. This bombardment is done by positive ions derived from an inert gas. Material is ejected from the target in such way that is possible to use quantities of the material which can be coated directly onto the substrate. Secondary electrons are also emitted from the target surface as a result of the ion bombardment. These secondary electrons play an important role because they maintain the plasma.

It must be noted that a number of criteria must be met in order to use this technique as a useful coating process. Ions with sufficient energy must be created and directed towards the surface of the target to eject atoms from the material (sputter). Also, ejected atoms must be able to move freely towards the object to be coated (substrate) with little resistance to their movements. This last one explains why the sputter coating is produced in a vacuum environment. Low pressures are required to maintain high ion energies and prevent too many atom-gas collisions after ejection from the target. The mean free path is the average distance the atoms can travel without colliding with another gas atom. Practical sputtering conditions must be such that the mean free path is not small compared with the target-substrate separation.

### 3.1 Magnetron Sputtering

Magnetron sputtering uses the principle of applying a specially shaped magnetic field to a diode sputtering target. Electrons within both fields experience the Lorentz force,

$$\vec{F} = -q(\vec{E} + \vec{v} \times \vec{B}) \quad (3.1)$$

where  $q$  and  $\vec{v}$  are the electron's charge and velocity respectively. If we consider a first case where  $\vec{B} \parallel \vec{E} \parallel \vec{v}$ , the emitted electron is influenced only by the electric field, which accelerates it. A second case is when the electric field is neglected. A launched electron at an angle ( $\theta$ ) with respect to  $\vec{B}$  now travels in a spiral motion with constant radius  $r$  and cyclotron frequency  $\omega$ ,

$$r = \frac{mv \sin \theta}{qB} \quad (3.2)$$

$$\omega = \frac{qB}{m} \quad (3.3)$$

The third case to consider is where electrons are launched at an angle to parallel uniform  $\vec{E}$  and  $\vec{B}$ . The electric field can be divided in the components perpendicular ( $E_{\perp}$ ) to the magnetic field and parallel ( $E_{\parallel}$ ) to the magnetic field.  $E_{\perp}$  and  $B$  make the electrons drift in the  $E \times B$  direction. The  $E_{\parallel}$  and  $B$ , on the other hand, make the electrons move to where the magnetic lines are parallel to the target surface, i.e., the gray circle in figure 3.1. It is here where the electron density is maximal.

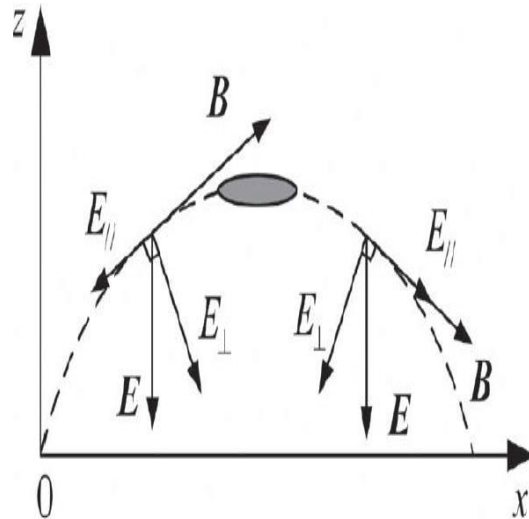


**Figure 3.1:** Electric and magnetic field directions in the right side of the magnetron cathode.

Figure 3.2 shows the magnets configuration for a magnetron cathode. One pole (North, for example) is positioned at the central axis of the target and the second pole (South) is formed by a series of magnets around the first pole and under the outer edge of the target. Trapping the electrons this way substantially increases the probability of an ionizing electron-atom collision occurring into an endless “race track”. This in turn causes the impedance of the plasma to drop and the magnetron source operates at low voltages.<sup>32</sup> This ionization efficiency leads to an increase in ion current density into the target that is proportional to the erosion rate of the target.

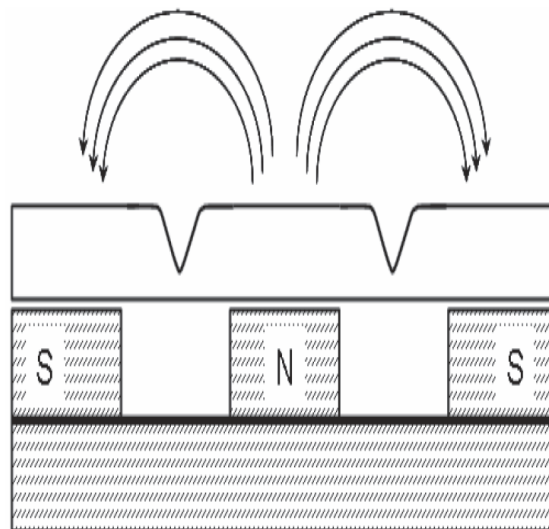


**Figure 3.2:** Typical profile for a magnetron cathode. Taken from [32].

## 3.2 Reactive Sputtering

Reactive sputtering is a deposition process where the deposited film is formed by a chemical reaction between the target material atoms and the reactive gas atoms. Some of the dielectric materials which are deposited by Radio-Frequency (RF) sputtering can be also deposited by reactive DC sputtering.

Usually, argon is introduced as the main sputtering gas while a small quantity of a second (reactive) gas is introduced into the chamber. The gas may be any gas which will react with the target to form a desired compound. Nitrogen and oxygen are the most common reactive gases used. Once these are injected, compounds are formed on both the target and substrate. By controlling the reactive gas flow, it is possible to control the composition of the growing film.

Although reactive sputtering is cheaper to implement than RF sputtering, it suffers from one important drawback called target "poisoning", which is the formation of a compound on its surface (an oxide if the reactive gas is oxygen). This poisoning leads to process instabilities which are related to hysteresis, arcing and the "disappearing anode" effect. These instabilities will be discussed later in this chapter.

## 3.3 Pulsed DC Magnetron Reactive Sputtering

Metallic materials can be readily deposited by DC magnetron sputtering. If the material to be deposited should be a dielectric, an RF sputtering method can be used. DC magnetron is the cheapest of the two general possibilities for sputtering because DC power supplies are simpler to manufacture and simpler to use. Deposition rates are also much higher with DC sputtering, for any given source power, than with RF sputtering. However, DC sputtering requires an electrically conducting target, and reactive DC sputtering introduces some difficulties which are discussed below. An alternative which can overcome some of the problems encountered when operating in reactive sputtering mode<sup>33</sup> is the use of a pulsed DC source, which was the approach followed in the present work.

As reactive DC sputtering occurs, areas on the metallic target become covered with insulating layers, as does the target's grounded shields. These coatings are produced by reaction of the target with the non-inert gas, namely oxygen in the present case, which is added to the sputtering gas (usually argon). This insulating layer now charges up until break down occurs in the form of an arc. These arcs affect the stoichiometry of the growing film and can even interrupt the process. Pulsing the target voltage polarity helps to prevent arcing. This dissipates the charges accumulated at the surface of the target through the plasma during the "pulse-off" period by switching the target voltage to a more positive value. In bipolar pulsed sputtering, the target voltage is actually reversed and becomes positive during the pulse-off period. In this part of the period, there is no deposition. Important distinctions with respect to RF sputtering is that in pulsed DC sputtering the frequencies employed are much lower and the power cycle is asymmetric, with only a relatively short portion of the time period in which the cathode polarity becomes actually positive.

During pulsed DC sputtering each pulse is divided in two segments the "on-time" ( $\tau_{\text{on}}$ ) and the "reverse-time" ( $\tau_{\text{rev}}$ ). The  $\tau_{\text{on}}$  is the duration of the negative voltage pulse applied to the magnetron (with respect to electrical ground) while the  $\tau_{\text{rev}}$  is the duration of the reversed pulse, during which the voltage to the magnetron is positive. If parameters are not selected properly, arcing will happen (if  $\tau_{\text{rev}}$  is too short, for example) or sputtering rate will be too low (if  $\tau_{\text{rev}}$  is too long). Figure 3.3 shows an ideal square pulsed DC signal supplied for the deposition process. In practice, actual signals can deviate quite significantly from this. Belkin *et al.* reported the effects of the selection of parameters for pulsed-DC reactive sputtering deposition of aluminum oxides.<sup>34</sup> Accumulation of charges occur during  $\tau_{\text{on}}$  as ions bombard the target. During the  $\tau_{\text{rev}}$ , electrons from the residual plasma discharge the layer. If the process of discharging is incomplete, a step-by-step charge accumulation happens throughout the sequential periods, eventually resulting in arcing.

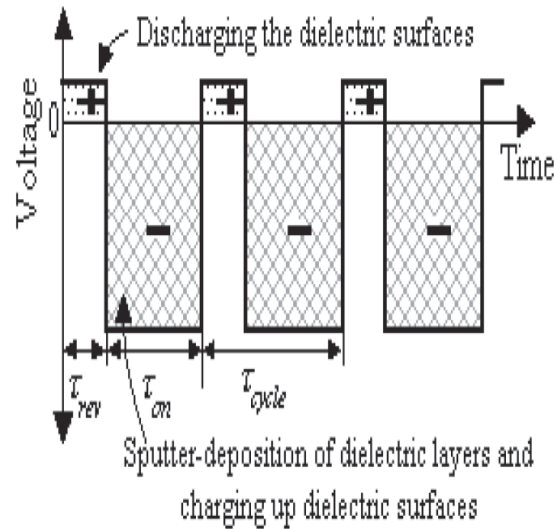


**Figure 3.3:** Representation of a periodic waveform of target voltage for a pulsed DC for a bipolar pulse mode. Taken from [34].

## 3.4 Instabilities in Reactive Sputtering

### 3.4.1 Hysteresis

As the reactive gas is injected to the chamber, it combines with the target material to form a compound. Ideally this reaction would take place only with the film growing on the substrate. In reality, it occurs also with the film being deposited on the chamber walls and any fixtures inside the chamber and, most importantly, with the target surface. Previous studies have reported that with increasing reactive gas flow an unstable transition can occur with the target switching uncontrollably from metallic to "poisoned" modes. This instability region may occur just in the pressure region where a desired composition for the film being deposited could be formed.<sup>35</sup> If this happens it will be very difficult to obtain this composition without taking special measures to achieve control. Figure 3.4 illustrates that the deposition process will become unstable if an increase in the reactive gas pressure results in a decrease in the reactive gas consumption.

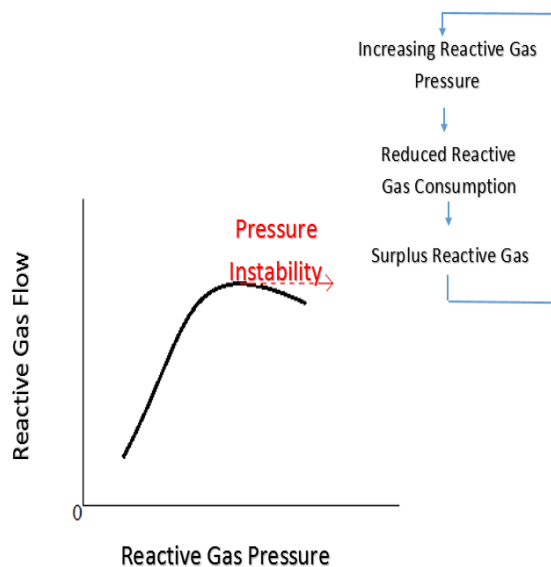


**Figure 3.4:** Instability in the system happens when an increased in pressure results from a decrease in reactive gas consumption. Based on diagram from [35].

One way to monitor this phenomenon is to observe the potential difference between target and ground as a function of reactive gas flow when the partial pressure of the reactive gas is the controlling variable. This voltage will change because target impedance with respect to ground is affected, which in turn depends on the extent of compound formation on its surface.

#### a) Results for Vanadium Pentoxide Target

In this work, a vanadium oxide target ( $V_2O_5$ ) of 99.9% purity was used to fabricate thin vanadium oxide films. To employ this target in the pulsed-DC magnetron gun, its operation parameters had to be adjusted due to the material's relatively low electrical conductivity. It was found that a frequency of 160 kHz with an inverse time of 1.5  $\mu$ s were adequate. Also, because of this target's low thermal conductivity and the possibility of damaging it through overheating, the following procedure was used: (1) Ignition of the plasma was done at a high argon pressure and low power (60 Watts), (2) power to the target was ramped at 10-20 Watts per minute until (3) low power operation was achieved for deposition (120 Watts) and, after the deposition, (4) a ramp-down procedure was performed similar to ramp-up, allowing the target to cool slowly to avoid thermal shock and potential target fracture. A background pressure of  $8.2 \times 10^{-7}$  Torr

was achieved to secure a clean environment. Working pressure was 6.2 mTorr, having an argon flow of 100 sccm and the target was pre-sputtered at 120 Watts for 30 minutes before deposition runs. These conditions ensured good stability in the system. It is noted that after pre-sputtering in pure argon, the target surface no longer consists of  $V_2O_5$  and it is expected to be partially metallized. For this reason, while the initial target is fully oxidized vanadium, it can still become necessary to inject oxygen during film growth.

A LabView program was used to monitor pressure, voltage, current, argon flow, oxygen flow and gun power while simultaneously displaying a graph of voltage as a function of oxygen flow. Oxygen was injected into the chamber at mass flows from 0 to 4 sccm, with intervals of 0.2 sccm. The results are shown in figure 3.4, in which three regions may be defined. The first part is labelled as the metallic region, even if this target is likely never fully metalized. Deposition process in this mode can be controlled easily, but the films fabricated under the metallic region will generally have a low concentration of oxygen. The second part is labelled as the reactive region. Once the reactive gas flow reaches a certain critical amount, the target begins to be oxidized more extensively and the voltage increases. Because of the accompanying hysteresis, it is difficult in this region to achieve a stable operation and, as a result, control of the film's composition will be poor. The third part is labelled as the oxidized region. The target is completely or mostly oxidized due to the insufficient removal of the insulating compound over the target's surface. In the oxidized region, the target is less conducting than in the metallic region, causing a voltage increase from 555 to 583 V. Moreover, the sputtering yield is expected to be reduced because atoms are more tightly bound in the oxides than in for metallic vanadium. The films which result from deposition conditions corresponding to the region beyond that labelled "reactive" in Fig. 3.5 will be more highly oxidized.

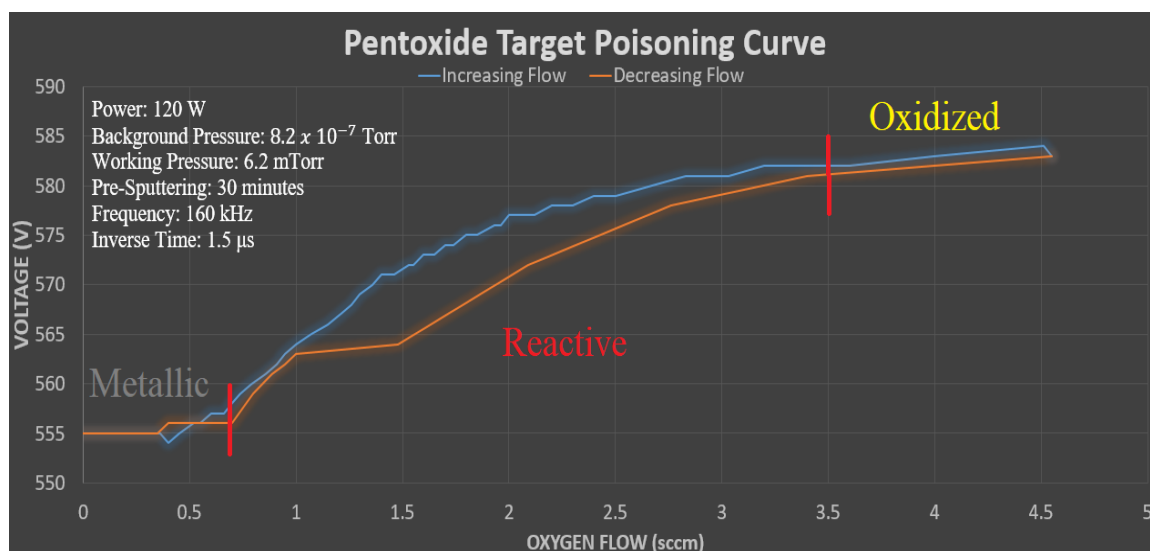


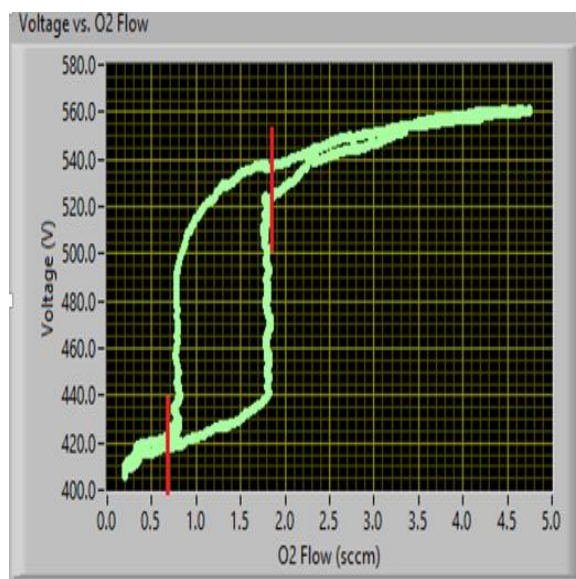
**Figure 3.5:** Poisoning of the Vanadium Pentoxide Target.

### b) Results for Vanadium Target

A pure metallic 99.5% vanadium target was also used in the present work. The pulsed-DC parameters were changed to a frequency of 5 kHz with inverse time of 0.4  $\mu$ s. Even though oxides form on the surface during reactive sputtering, a small  $\tau_{rev}$  is enough to discharge the metallic target. Curves of voltage vs. oxygen flow were obtained to study the relationship between the three regions (metallic, reactive and oxidized) and deposition parameters like working pressure, argon flow and gun power. A LabView program was used to monitor the same parameters as with the pentoxide target.

Background Pressure (Torr)	Working Pressure (mTorr)	Argon Flow (sccm)	Gun Power (Watts)	Pre-Sputtering (min)
$4.4 \times 10^{-7}$	6.2	25	200	30

**Table #1:** Stability conditions for 6.2 mTorr working pressure film deposition.



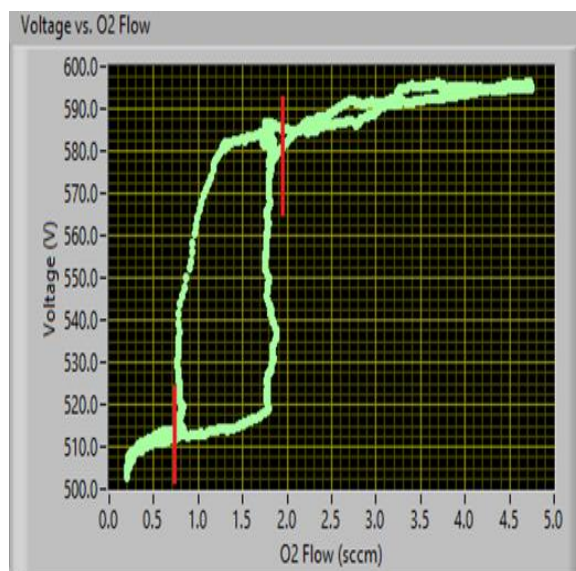
**Figure 3.6:** Voltage as a function of oxygen flow for 6.2 mTorr film deposition.

Table #1 shows stability conditions for figure 3.6 before the oxygen injection. Oxygen flow was increased from 0 to 4.5 sccm at intervals of 0.2 sccm. At a 6.2 mTorr working pressure, the metallic region extends from 0 to 0.7 sccm, the reactive region presents a change between 440 and 520 V and the oxidized region extends from 2 to 4.5. As the flow was reduced from 4.5 sccm back to zero, hysteretic behaviour was clearly observed, as shown in figure 3.5.

Table #2 shows stability conditions for the case in figure 3.7 before the oxygen injection. In contrast with the previous case, working pressure was increased from 6.2 to 20.2 mTorr. The purpose was to observe if an increase in working pressure would affect the curve's behaviour. As seen in figure 3.7, the metallic region ranges from 0 to 0.7 sccm, the reactive region presents a cathode voltage change from 520 to 580 V, and then the oxidized region ranges from 2 to 4.5 sccm. Compared to figure 3.5 which was done at 6.2 mTorr Ar working pressure, increasing the working pressure to 20.2 mTorr did not produce any variation on the metallic, reactive and oxidized regions. Therefore, it was determined to work under 6.2 mTorr Ar pressure.

Background Pressure (Torr)	Working Pressure (mTorr)	Argon Flow (sccm)	Gun Power (Watts)	Pre-Sputtering (min)
$4.7 \times 10^{-7}$	20.2	25	200	30

**Table #2:** Stability conditions for 20.2 mTorr working pressure film deposition.



**Figure 3.7:** Voltage as a function of oxygen flow for 20.2 mTorr working pressure film deposition.

Table #3 shows stability conditions for figure 3.8 before oxygen injection. The difference between previous tests is the increase of argon flow from 25 to 100 sccm. Interestingly, the metallic region extends from 0 to 1.2 sccm and the reactive region displays a vertical width of only ~3 V. This value in the reactive region implies that the region achieves much better stabilization than for the other cases and control of film composition should be more easily achieved. The reduction or elimination of the hysteretic effect has been previously studied, theoretically and experimentally by different authors.<sup>36-40</sup>

Background Pressure (Torr)	Working Pressure (mTorr)	Argon Flow (sccm)	Gun Power (Watts)	Pre-Sputtering (min)
$5.7 \times 10^{-7}$	6.2	100	200	30

**Table #3:** Stability conditions for 6.2 mTorr working pressure with 100 sccm argon flow film deposition.

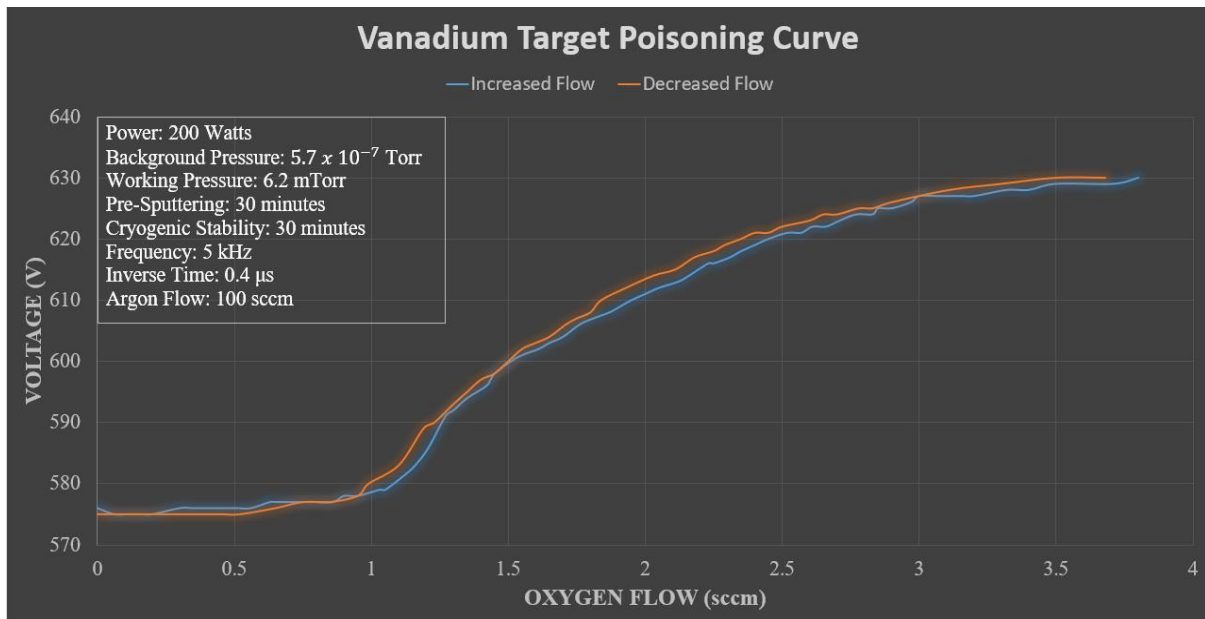


**Figure 3.8:** Voltage as a function of oxygen flow for vanadium target. Increasing the argon flow prevents hysteresis and increases the stable region.

In previous cases, gun power was fixed at 200 Watts. It was of interest to study the behaviour of the voltage as a function of the oxygen flow while power was varied to 100, 200 and 300 Watts using a working pressure of 6.2 mTorr and argon flow of 100 sccm. From the results shown in figure 3.9, an increase in power causes an increase in range of the metallic region. At 100 Watts, the metallic region stops at 0.3 sccm of oxygen flow while at 300 Watts, it stops at 2.0 sccm. This is explained by the fact that a higher power translates to higher number of argon ions hitting the target per unit time. Target material atoms are being sputtered faster, which prevents oxidation, resulting in a longer metallic portion in the curve.

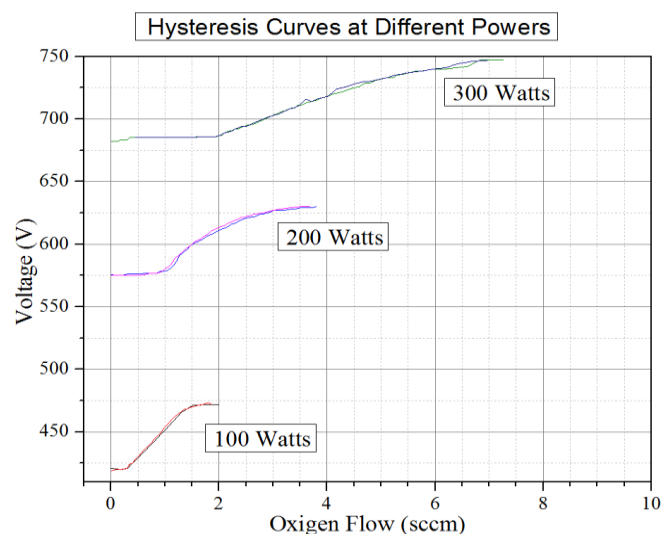


**Figure 3.9:** An increase in power results in a lengthening of the "metallic" region.

### 3.4.2 Arcing

Arcing during reactive sputtering is a very challenging issue. These arcs can be defined as high-current electrical discharges from the cathode. This phenomenon becomes more severe when the compound is highly insulating (or a metal target is poisoned) and when the deposition is done with high target current.

Arcs are distinguished by a focused and localized discharge by a collective electron emission from a breakdown event.<sup>41</sup> Insulating defects can occur on a target's uneroded surface for different reasons. For one, the build-up of a compound insulating layer over a metallic target surface due to a reactive gas. Secondly, impurities possibly found in the dielectric or metallic targets. The insulating layer and impurities result in localized charge accumulation in DC sputtering. Energy concentrated at the sites can be sufficient to form molten material at the arc's location. These conditions generate the perfect background for explosive ejection of matter from the region in the form of macro-particles.

The formation and ejection of macro-particles can be one of the most damaging consequences of arcing. It can occur while sputtering with any material in any given ambient gas. Also, arcing disrupts the uniform and continuous power delivery to the target. This behaviour can reduce deposition rates and produce non-uniformity in thin film fabrication.

### 3.4.3 Disappearing Anode

Another effect influencing reactive sputtering is the phenomenon of anode degradation or "disappearing anode". Dielectric material is deposited not only over the substrate but also over the chamber walls and the anode. The insulating layer now prevents the anode to operate as ground. In consequence, this area ceases to be an effective anode and the plasma will shift to find a new, lower resistance anode. This shifting results in a pattern change over the magnetron deposition. It must be pointed out that this effect does not become significant until the entire anode vanishes (becomes completely coated with dielectric material). Solutions to this problem

are (1) a dual magnetron system<sup>42</sup> and (2) mechanical cleaning of the anode before each deposition. For the present work, since the oxides being deposited are not good conductors, it was important to clean the anode frequently.

### 3.5 Consequences of Target Erosion in Reactive Sputtering

The majority of the collisions between the target and the ions occur at about half the target radius in a circular magnetron gun.<sup>43</sup> The erosion develops a “race track” which is dependent on the strength of the cathode’s voltage and the local magnetic field. An increase in magnetic field strength will make the race track narrower, while a voltage increase will broaden the race track.<sup>44</sup> If the depth of the race track approaches the thickness of the target, the target can no longer be used without risking damage to the gun and introducing contaminants to the coating. A complete study on target erosion was performed by Schoff for a copper target.<sup>45</sup> No target erosion study has been made for Pulsed-DC Magnetron reactive sputtering targets, although results are expected to be similar.

For our work, initial thickness of the vanadium target used was 6.35 mm, but as the target is used, thickness along the racetrack is reduced. Curves of the cathode voltage vs. oxygen flow rate, as shown in Section 3.4.1, were performed for a target which had been used for many hours, so it already had a noticeable racetrack. Its depth was not measured at that time, however. Afterwards, it was noticed that growth conditions previously found to produce films with a particular composition would not yield reproducible results after the target had been used for a longer time. In order to explore the effect of racetrack depth a voltage vs. oxygen flow rate cycle was measured again with a target near the end of its useful life (0.75 mm thickness at the bottom of the racetrack). The result is shown in Figure 3.10 for this case, along with a previous result for a much thicker target (but with unknown racetrack depth). In both cases the target power was 200 Watts and the argon flow was 100 sccm. The upper limit of the “metallic” region for the thinner target extends only up to ~1.5 sccm instead of ~2.5 sccm. This means

that the target appears to become more easily oxidized as it becomes thinner. In terms of composition, this suggests that a lower oxygen flow may be then required in order to reproduce films with a particular oxidation state. For a thicker target, cathode voltage in the reactive region changes more sharply as a function of oxygen flux, particularly at lower fluxes (under ~6 sccm) while a smoother increase is observed for the thinner target. The total voltage change from zero oxygen flow up to the maximum attempted is also noticeably larger for the thicker target.

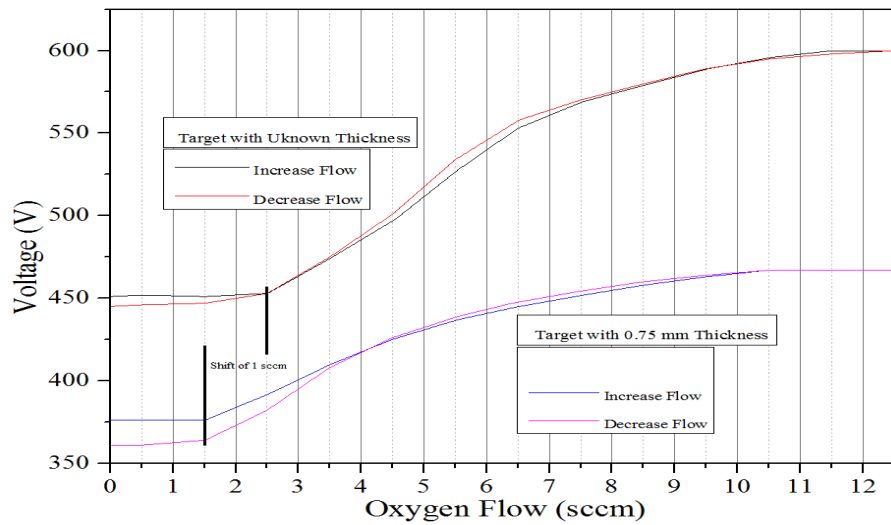


**Figure 3.10:** Voltage as a function of oxygen flow for the target at 0.75 mm thickness and at a larger unknown thickness.

## Chapter 4 Experimental Procedures

### 4.1 Substrates

Most samples were grown on SiO<sub>2</sub> glass substrates. The size of the heater inside the chamber determined that a 20mm X 10mm substrate cut from the original size was adequate for film growth. For cleaning, substrates were placed in 15 mL of trichloroethylene and sonicated for 10 minutes, followed by 10 minutes in 15 mL of acetone and 10 minutes in 15 mL of methanol. Substrates were left to air dry after the bath. Subsequently, storage in individual containers was done to prevent contamination.

A small silicon wafer was attached with silver paint to the edge of the substrate for the purpose of measuring, after the deposition, the thickness of the film with a profilometer. The substrate was similarly attached over a 1.6 mm thick copper disc of 25.6 mm in diameter and the disc was then attached to the ceramic heater inside the deposition chamber. This configuration allowed a more uniform heat distribution through the substrate. The temperature of the ceramic heater was increased to 50 °C for 10 minutes to dry the silver paint and improve thermal contact between the substrate, the disk and the heater.

### 4.2 Cryogenic Vacuum Pump

The main vacuum pump of the deposition system is an APD Cryogenics helium cycle cryopump. A cryopump captures the gas by condensation to internal surfaces cooled to very low temperatures. An appropriate medium-vacuum pressure must be provided inside the volume to be evacuated, usually with a mechanical pump before the cryopump can be started. The entrapment effect is a consequence of the interaction between the gas molecules to be pumped and a cold surface (the cryopanel), which is cooled by internal contact with helium gas which has been cooled by the cryopump's refrigerator.

The cryopump operates on the principle of closed-cycle refrigeration. The system consists of a helium compressor, a cryopump proper and interconnecting helium lines. Inside the pump,

there is a motor-driven multi-stage piston assembly called a displacer. It contains expanders which are two-stage cryogenic refrigerators that operate on the Gifford-McMahon refrigeration cycle. Compressed helium from the compressor flows into the piston assembly. As the piston moves up, the helium gas expands and cools. Once the piston starts moving down, it pushes the helium out of the cryopump and back to the compressor. The helium is re-compressed and the cycle repeats. In each cycle, more heat is removed from the arrays and the cryopanel continue to cool down.

As seen in figure 4.1, the first-stage outer cryopanel are cooled to 50 to 70 K.<sup>46</sup> Here, most of the water vapor present in the deposition chamber freezes. These cryopanel also act as a heat shield between the vacuum enclosure, the louver and the second-stage cryopanel. At the second stage, the cryopanel reach a working temperature of 20 to 30 K. These inner panels freeze out nitrogen, oxygen and argon after they pass through the louver. Remaining gasses like neon, hydrogen and helium which do not freeze even at the second-stage, are adsorbed by charcoal traps inside the cryopanel.

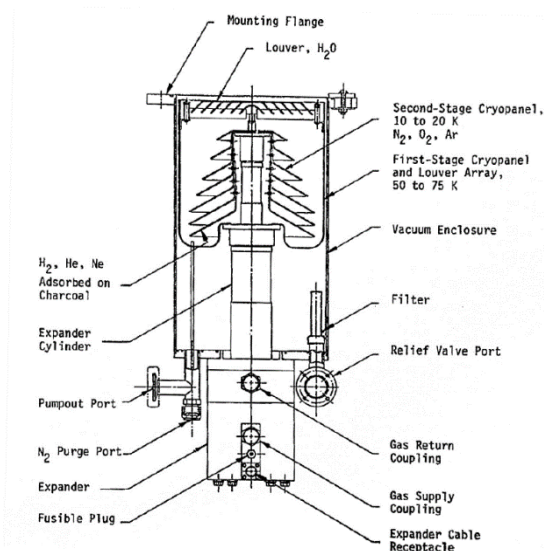


**Figure 4.1:** Diagram and sections of the cryopump. Taken from [46].

### 4.2.1 Regeneration

Cryopumps retain pumped gasses as long as their capacity is not exceeded, and the arrays are maintained at appropriate temperatures. The condition of a saturated cryopump may arise

when the cryopanel's temperature are too high due to temperature gradients or when the cryodeposit condensed at the baffle blocks the louver. Once the capacity limit has been reached, the cryopump must be regenerated.

Regeneration was regularly done in the present case by turning off the pump and heating the outside body of the pump. The surface was wrapped in a heating strip connected to a variable output transformer used as power supply, which allowed control over the temperature of the strip. Relatively weak forces are involved between the gasses and cryopanel and do not include chemical bonds. Consequently, cryopumps do not require high temperatures for regeneration. Before heating, the gate valve between the pump and the deposition system was closed. As a result, the pressure in the pump increases strongly, so that the gas could be pumped away by the mechanical pump. The body of the cryogenic pump was heated to extract any water condensation accumulated on the cryopanel while simultaneously being pumped down to a pressure of 30 mTorr. After pumping the released gasses, the cryopump was left to cool down to room temperature and it was then ready to be used for the next pumping period.

### **4.3 Deposition Chamber**

The interior walls of the deposition chamber were cleaned with propanol after every five film depositions. Material is deposited not only over the substrate but also the chamber and anode are covered by coating. This is undesirable, particularly when the coatings are dielectric or poorly-conductive, because electrical characteristics of the system then change over time and, particularly if the anode becomes covered, which leads to raising its potential with respect to ground, the phenomenon known as the disappearing anode effect, as discussed previously in Section 3.4.3.

A gate valve separates the deposition chamber from the cryopump. Before using the cryopump, a minimum "crossover" pressure had to be achieved inside the chamber. To this end, a Varian SD-201 mechanical pump was used for roughing. The crossover pressure is that

at which the cryopump can work without becoming rapidly saturated. The isolating gate valve is only opened to begin steady cryopumping of the main vacuum chamber once the chamber pressure has reached a value under this minimum. To determine the maximum crossover pressure, the following formula was used,

$$\text{Crossover Pressure (torr)} \leq \frac{\text{Pump Crossover Rating (torr-liters)}}{\text{Chamber Volume (liters)}} \quad (4.1)$$

The crossover rating is given by the cryopump manufacturers (220 torr-liters for the pump used). The chamber in our system has a volume of approximately 50 liters. The main chamber was rough pumped down to 20-30 mTorr, which is well below the maximum crossover pressure. After reaching this pressure, the valve separating the mechanical pump from the chamber was closed and the pneumatic sliding gate valve was opened. As a consequence, pressure drops very rapidly from 20 mTorr to 100  $\mu$ Torr. After approximately fifteen minutes of cryogenic pumping, pressure drops to 0.1  $\mu$ Torr. A Residual Gas Analyzer (RGA) was used to monitor the background pressure and the residual gasses. Figure 4.2 is shown as an example of the background pressure and the residual gas analysis before a deposition. Most of the base pressure is composed of water vapor.

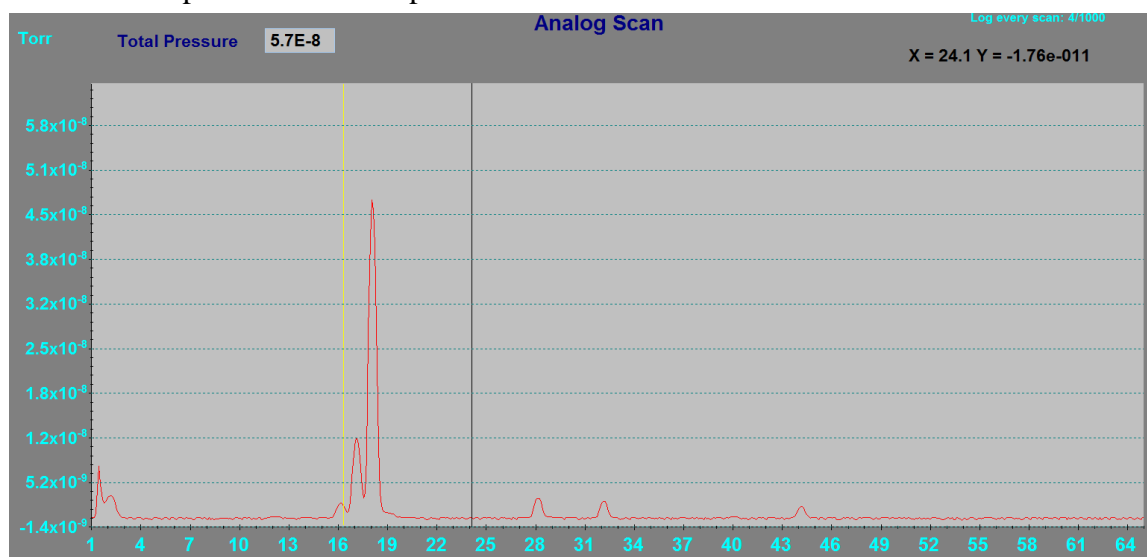


**Figure 4.2:** Residual gas analysis from the RGA shows base pressure is mostly composed of air and water vapor. Background pressure is  $5.7 \times 10^{-8}$  Torr in this case, which was measured after 15 minutes of cryopumping the vacuum chamber.

## 4.4 Ceramic Heater

The temperature of the ceramic heater was controlled by a Honeywell UDC 2500 temperature controller. The controller uses a K-type thermocouple placed underneath but inside the ceramic heater to measure the temperature. Since the temperature of the substrate is not the same as that of the heater, a calibration curve was made to determine the actual temperature at the substrate's surface.

Two substrates were attached with silver paint in a "sandwich" like manner. At the center of the top substrate, a small hole was drilled. A K-type thermocouple was placed inside the hole, making contact with the bottom substrate's surface. This thermocouple was connected to an Omega HH-20A High Accuracy Digital Thermometer. The chamber was prepared as if the deposition was to be made and the temperature of the controller was increased by 50 °C. Once the selected temperature was reached, 10 minutes were allowed for the temperature to stabilize before taking into account the controller's temperature and the substrate's surface temperature. Figure 4.3 shows the resulting calibration curve, which was then used to estimate the actual temperature for the growing film in each deposition. The equation used to estimate the temperature was the following,

$$y = 0.8938x + 40.466 \quad (4.2)$$

where  $x$  is the controller's temperature and  $y$  is the substrate's surface temperature.

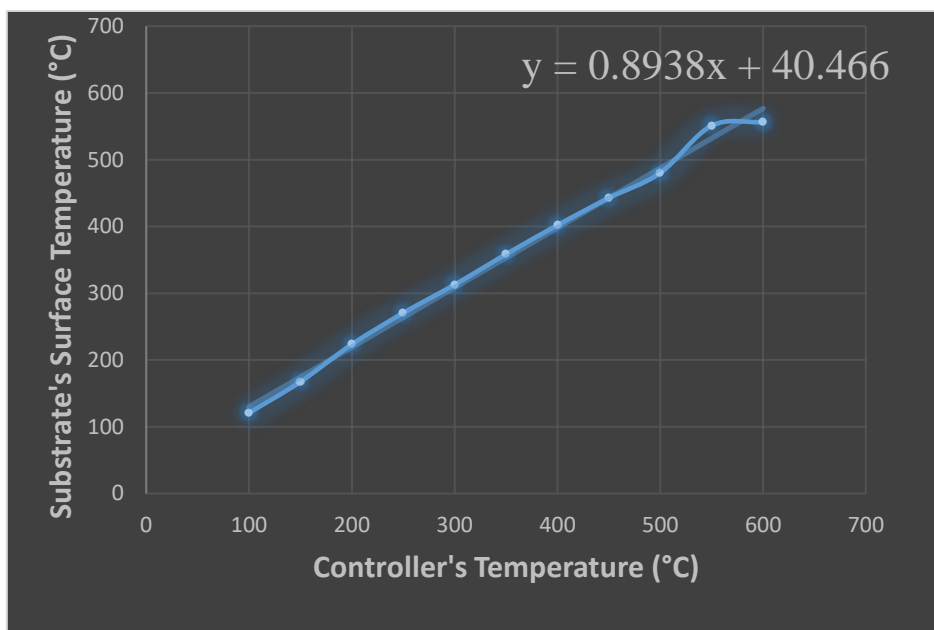


**Figure 4.3:** Result of the calibration between the controller and substrate's surface temperature.

## 4.5 Argon and Oxygen Atmosphere Pre-Sputtering

Working pressures were 5.0 or 6.2 mTorr argon for the samples. This pressure range is adequate for most sputter-deposition work with magnetron guns, providing a good compromise between sputtering yield and kinetic energy of sputtered atoms.<sup>47</sup> The argon pressure was controlled using a diaphragm valve situated between the cryopump and the pneumatic gate valve. At this point, the pressure was monitored by an Agilent CDG-500 vacuum gauge. The argon flow was kept constant at 100 sccm flow using an MKS Mass Flow Controller. A pre-sputtering of 5 minutes was allowed to clean the target from impurities and for the argon pressure to stabilize.

Oxygen was injected into the chamber once the argon pressure was stable. Oxygen flow was adjusted by another MKS Mass Flow Controller. Throughout the sample runs, flow was varied to obtain a diversity of vanadium oxides. Although the oxygen flow was always less than that of argon, oxygen fraction in the chamber's atmosphere is known to have a significant effect on the resulting films.<sup>48</sup> A total of 10 minutes sputtering was allowed for stabilization of Ar/O<sub>2</sub> mixture before removing the shutter to begin deposition.

## 4.6 Characterization Techniques

### 4.6.1 X-ray Diffraction

X-ray diffraction (XRD) is a powerful non-destructive technique for characterizing crystalline materials. It provides information on crystal structure, phase, crystal orientation, average grain size, crystallinity, strain and crystal defects. X-ray diffraction patterns are the fingerprint of the periodic atomic arrangement in any given material.

In 1912, Max von Laue discovered that crystalline substances act as three-dimensional diffraction gratings for X-ray wavelengths similar to the spacing of planes in a crystal lattice.<sup>49</sup> X-rays are generated in a cathode ray tube by heating a filament to produce electrons. Electrons are then accelerated towards a target (Cu, Fe, Mo or Cr usually) by applying a voltage. When the electrons have sufficient energy to dislodge inner shell electrons of the target, characteristic X-ray spectra are produced.

The X-rays are collimated and directed toward the sample. The interaction of the incident rays with the sample can produce constructive interference when conditions satisfy the following equation,

$$n\lambda = 2d \sin \theta , \quad (4.3)$$

known as Bragg's Law. Figure 4.4 shows, schematically, X-ray diffraction from a single crystal. Bragg's law relates the wavelength ( $\lambda$ ) of electromagnetic radiation to the diffraction angle ( $\theta$ ) and the lattice spacing ( $d$ ) in a crystalline sample. In a diffractometer, these diffracted rays are then counted by a detector and the diffraction angles are accurately measured.

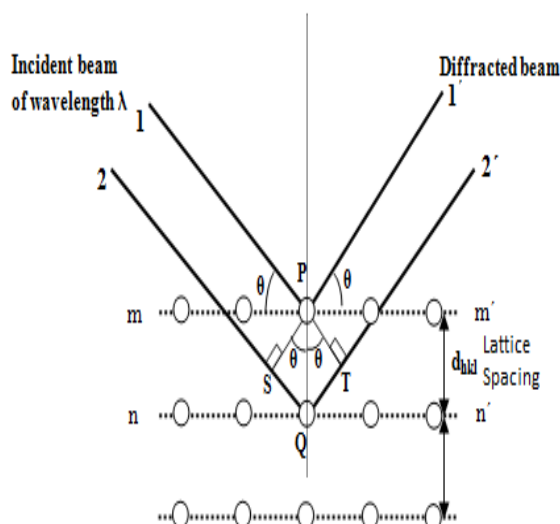


**Figure 4.4:** Braggs X-ray Reflection.

The lattice spacing is in the order of Angstroms. This distance is slightly larger than the X-ray wavelengths commonly used. Scanning the sample through a range of  $2\theta$ -angles, all possible diffraction directions of the lattice can be obtained if the sample is composed of totally randomly oriented crystals, such as in fine powders. Converting the diffraction peak angles dictated by the d-spacings allows the identification of the material. In the present application, microcrystals in films are not necessarily randomly oriented, and in some cases, are highly oriented, so not all diffraction peaks may be observed.

In addition, based on the width of the diffraction peak, the average vertical grain size for the samples was calculated using Scherrer's equation,<sup>50</sup>

$$\tau = \frac{0.94 \cdot \lambda}{b \cdot \cos \theta} \quad (4.4)$$

where  $b$  is the full width at half maximum of the diffraction peak (FWHM),  $\theta$  is Bragg's angle for the selected peak and  $\lambda$  is the wavelength of the radiation used.

XRD analysis in this work was carried out using a Bruker D8-Discover diffractometer. X-rays were produced from a copper target, which yields a main radiation peak with  $1.5418 \text{ \AA}$  wavelength ( $\text{CuK}_\alpha$  radiation). The target was bombarded with a 40-mA electron beam accelerated through a potential difference of 40 kV.

### 4.6.2 Atomic Force Microscope

The Atomic Force Microscope (AFM) is similar to a stylus profilometer but is much more sensitive and is able to scan over sample areas and provide topographic maps. A probe in the form of a fine tip at the end of a microcantilever is used to scan over the sample in such a way that it, ideally, does not damage the surface of the sample. This instrument has been demonstrated to have up to atomic resolution at least with some types of samples, but is much more often used at lower resolutions.<sup>51</sup> The spring of the AFM cantilever beam is a critical parameter. It must be as soft as possible to maximize deflection for a given force while simultaneously being stiff enough to minimize vibrations from the surrounding environment. In its most common implementation the AFM images are obtained by the measurement of the displacement of the cantilever tip interacting with the surface of the sample. When the tip is moved, it will follow the topography of the sample's surface.

The AFM provides a three-dimensional surface profile. In addition, the samples do not require any special treatment that would change or damage irreversibly the sample and can be done perfectly in ambient air. A selected number of samples were analysed by this technique to study the relationship between grain size and electrical measurements. Also, it was used to compare how grain size and shape for different vanadium oxides phases.

### 4.6.3 Electrical Measurements – Resistance and Resistivity

Electrical measurements at different temperatures play an important role in material characterization, particularly for semiconductors. Electrical resistivity is an intrinsic characteristic of the material that quantifies how strongly a given material opposes the flow of electric current. The most common way of measuring the resistivity of a semiconductor material is with the four-point probe technique in a van der Pauw configuration, as illustrated in figure 4.5. It involves applying a current through two of the probes while measuring voltage

using the other two. The van der Pauw method is preferred for small thin film samples and was therefore the one used in the present work.

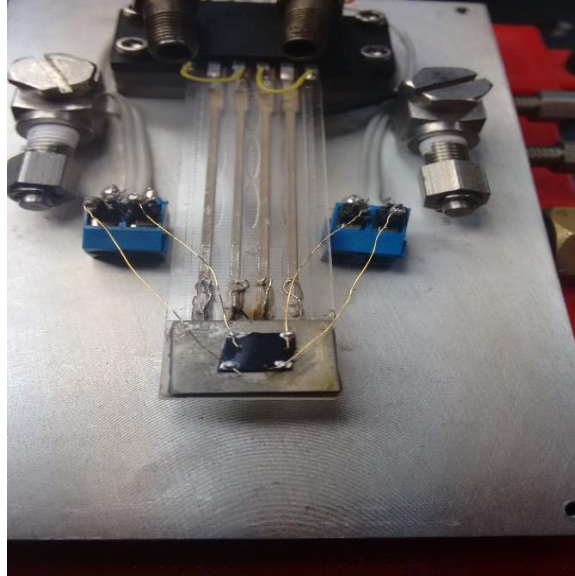


**Figure 4.5:** Resistivity measurement configuration for the samples.

A square measuring ~10 mm on the side was cut from the original samples in order to perform the resistivity measurements. This size was dictated by the size of the Peltier heater in the resistance test chamber. Silver grease was applied between the heater and the sample. Four thin gold strings were attached with a small amount of silver paint on the periphery of the sample to make the contacts. The size of the contacts was made as small as possible, since contact size has an effect over the electrical measurements.<sup>52</sup>

The resistivity is derived from a total of eight measurements that are made around the periphery of the sample. The resistance is defined using Ohm's Law,

$$R_{kl,mn} = \frac{V_{m,n}}{i_{k,l}} \quad (4.5)$$

The subscripts  $m, n, k, l$  specifies the number corresponding to a vertex in the sample, as shown in figure 4.6.  $V_{m,n}$  is the voltage measured between contacts  $V_m$  and  $V_n$  when a current  $I_{k,l}$  is passing through the contacts  $I_k$  and  $I_l$ . In general,  $k, l$  and  $m, n$  are two consecutive contact points (numbered along the edge of sample) between which the current is applied ( $i_{kl}$ ) and the other

two, between which voltage is measured ( $V_{mn}$ ). The resistance of the sample can be determined from two of these resistances, with a first measurement with current applied between, for example, points 1 and 2, and a second measurement with current applied between points 2 and 3, but for better accuracy it is necessary to perform similar measurements along different pairs of contacts, as described below. With reference to figure 4.6, horizontal contact points measurements are  $R_{12,34}$  and  $R_{34,12}$  while vertical contacts points measurements are  $R_{23,41}$  and  $R_{41,23}$ . For further improvement in the accuracy of the resistance values, measurements were done after switching polarities of the current source. Combining all the previous conditions leads to the following formulas,

$$R_{horizontal} = \frac{R_{12,34} + R_{34,12} + R_{21,43} + R_{43,21}}{4} \quad (4.6)$$

$$R_{vertical} = \frac{R_{23,41} + R_{41,23} + R_{32,14} + R_{14,32}}{4} \quad (4.7)$$

Van der Pauw demonstrated that, knowing both resistances and the thickness of the sample, the resistivity could be solved from:

$$e^{-\frac{\pi d}{\rho} R_{horizontal}} + e^{-\frac{\pi d}{\rho} R_{vertical}} = 1 \quad (4.8)$$

It can be shown then that

$$\rho = \frac{\pi d}{\ln 2} \cdot \frac{R_{horizontal} + R_{vertical}}{2} f \quad (4.9)$$

where  $f$  is a correction factor which is a function only of the ratio of the horizontal and vertical resistances and satisfies the transcendental equation,<sup>52-54</sup>

$$\cosh\left\{\frac{(R_{horizontal}/R_{vertical})-1}{(R_{horizontal}/R_{vertical})+1} \frac{\ln 2}{f}\right\} = \frac{1}{2} e^{\frac{\ln 2}{f}} \quad (4.10)$$

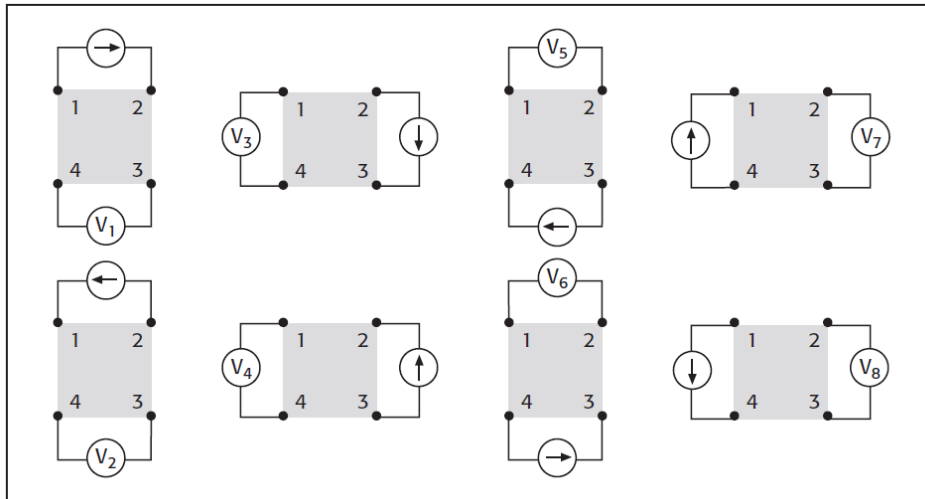


**Figure 4.6:** Diagram of the eight van der Pauw measurements. Arrow represents the direction of the current.

Taken from [54].

## Chapter 5 Results and Discussion

In this chapter, the results obtained for VO<sub>2</sub> (B) samples will be discussed. All X-Ray diffraction patterns, electrical measurements and atomic force microscope characterization results discussed in this chapter were obtained by the methods mentioned in the previous chapter.

### 5.1 X-ray Diffraction (XRD) Analysis

Based on preliminary experiments of deposition with varying oxygen flow, only the results for samples deposited with O<sub>2</sub> flows of 11.5 or 12.5 sccm will be discussed because these are the cases for which B-phase VO<sub>2</sub> was obtained. A total of 10 samples were fabricated at different temperatures, deposition time and substrate types. Table 5.1 summarizes each sample's deposition parameters.

Sample	Working Pressure Ar (mTorr)	Oxygen Flow (sccm)	Deposition Temperature (°C)	Time (min)	Substrate	•Resulting Phase
J127	5.00	12.5	375	30	SiO <sub>2</sub>	VO <sub>2</sub> (M <sub>1</sub> )
J128	5.00	12.5	350	30	SiO <sub>2</sub>	VO <sub>2</sub> (B)
J129	5.00	12.5	350	30	SrTiO <sub>3</sub>	VO <sub>2</sub> (B)
J130	5.00	12.5	350	30	SiO <sub>2</sub>	VO <sub>2</sub> (B)
J131	5.00	12.5	325	30	SiO <sub>2</sub>	Mix
J132	5.00	12.5	375	30	SrTiO <sub>3</sub>	Mix
J162	5.00	11.5	350	30	SiO <sub>2</sub>	VO <sub>2</sub> (B)
J163	5.00	11.5	350	15	SiO <sub>2</sub>	VO <sub>2</sub> (B)
J164	5.00	11.5	350	45	SiO <sub>2</sub>	VO <sub>2</sub> (B)
J165	5.00	11.5	375	15	SiO <sub>2</sub>	VO <sub>2</sub> (B)

**Table 5.1:** Deposition parameters for VO<sub>2</sub> (B) phase samples.

VO<sub>2</sub> (B) has a low-symmetry monoclinic structure (space group  $C2/m$ )<sup>54</sup> with lattice constants  $a = 12.03 \text{ \AA}$ ,  $b = 3.69 \text{ \AA}$ ,  $c = 6.42 \text{ \AA}$  and  $\beta = 106.6^\circ$ . Samples J128 and J130, deposited at the same nominal conditions, show very similar X-ray diffraction patterns. From figure 5.1, there are three sharp and strong peaks at  $14.44^\circ$ ,  $29.04^\circ$  and  $44.14^\circ$  which can be indexed,

• Based on X-ray diffraction characterization only.

respectively, to the (001), (002) and (003) reflections of this monoclinic phase. The intensity of these peaks means that the VO<sub>2</sub> (B) films have strong preferential crystallization orientation with (001) planes growing parallel to the substrate surface. Table 5.2 shows the calculated perpendicular grain size using Scherrer's equation. Based on the width of the X-ray peak at (002), the crystal grain size perpendicular to the surface of samples J128 and J130 are ~38 and ~36 nm respectively. A closer inspection of the result for sample J128 reveals small peaks after 20 degrees which may be attributed to V<sub>4</sub>O<sub>7</sub> or other lower oxides.

Sample	Perpendicular Grain Size (nm)
J127	42.5
J128	38.2
J129	19.7
J130	35.7
J131	39.6
J132	50.4
J162	42.0
J163	39.7
J164	42.2
J165	41.0

**Table 5.2:** Perpendicular grain sizes for all samples.

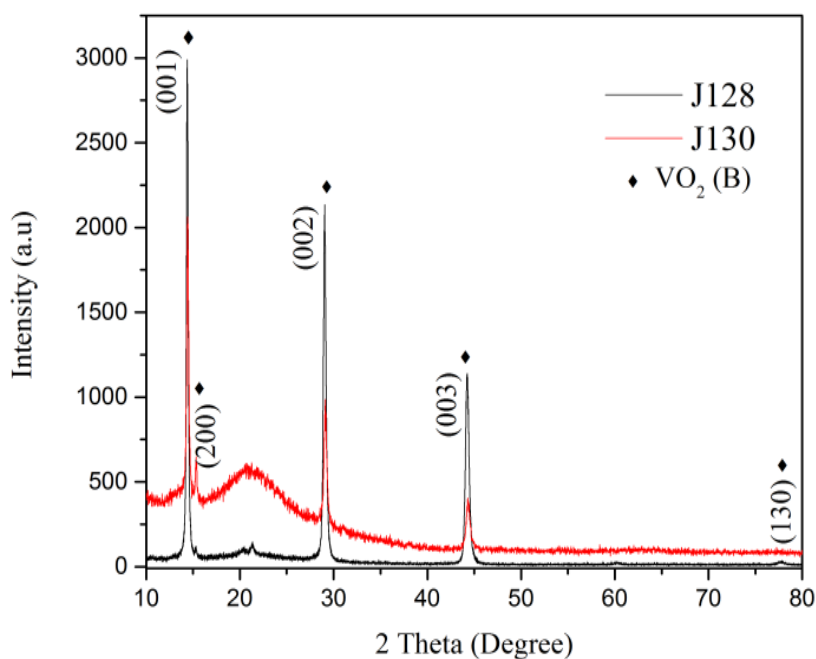


**Figure 5.1:** X-Ray diffraction 2-Theta patterns for samples J128 and J130.

The influence of deposition temperature over the resulting phase was also investigated. Maintaining a constant oxygen flow of 12.5 sccm, temperature was varied from 375 to 325 °C at intervals of 25 degrees. As shown in figure 5.3, temperature plays a significant role in film oxidation and also in the resulting phase for VO<sub>2</sub>. A peak at 27.78°, which is assigned to VO<sub>2</sub> (M<sub>1</sub>), appears as the deposition temperature was increased to 375°C. As shown later, measurement of electrical characteristics confirmed that it was indeed the case that the M<sub>1</sub> phase was present. Consequently, a difference of just 25 degrees in deposition temperature may determine whether the VO<sub>2</sub> (M<sub>1</sub>) or VO<sub>2</sub> (B) phase is obtained. On the other hand, a further decrease in growth temperature allows the co-existence of different vanadium oxide phases, as peaks for V<sub>4</sub>O<sub>7</sub> and V<sub>4</sub>O<sub>9</sub> begin to appear, as shown in Fig 5.2 for sample J131. Therefore, the lower growth temperature inhibits oxidation.

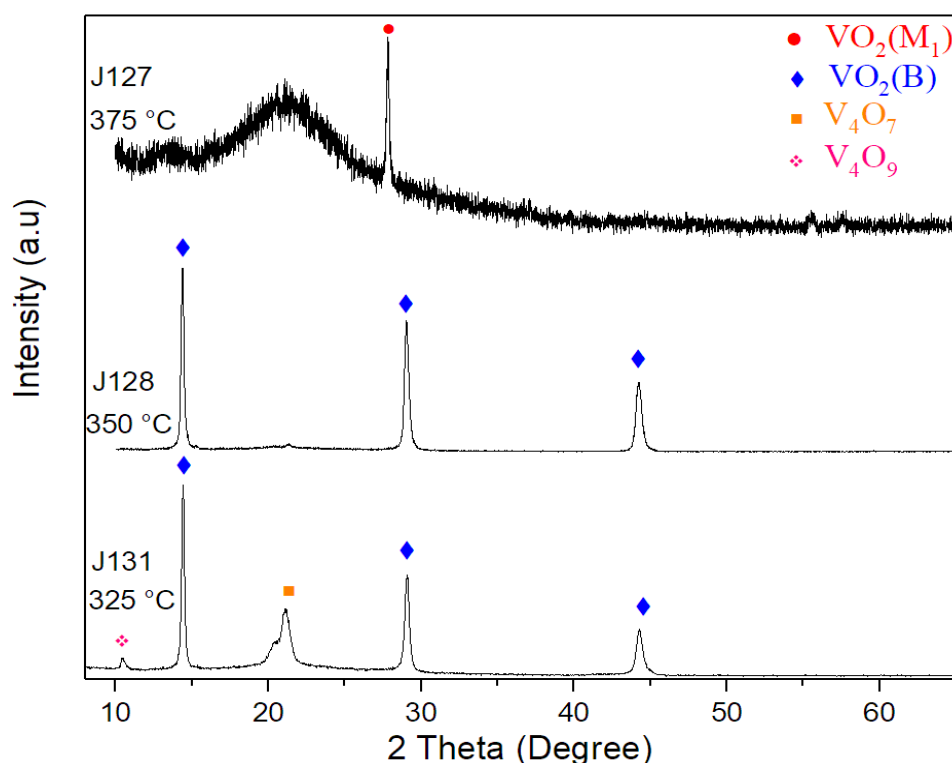


**Figure 5.2:** X-Ray diffraction patterns for samples grown at different temperatures, with 12.5 sccm O<sub>2</sub> flow.

Samples were also grown on SrTiO<sub>3</sub> (STO), a perovskite-type structure substrate, with crystallographic orientation (001). Growth temperatures were 350 and 375 °C (samples J129 and J132, respectively in Table 5.1). It has been shown that VO<sub>2</sub> (B) thin films grown by pulsed

laser deposition can be lattice-matched to (001)-cut STO substrates.<sup>56</sup> Thus, it seemed of interest to explore this possibility of stabilizing VO<sub>2</sub> (B) phase for films grown by DC magnetron sputtering method using the same conditions as for the amorphous SiO<sub>2</sub> substrates. As seen in figure 5.3, (001)-oriented VO<sub>2</sub> (B) is in fact obtained, but a VO<sub>2</sub> (M<sub>1</sub>) peak at 27.8° was observed for the sample grown at the higher deposition temperature. Peaks at 14.3° and 28.9° in these scans can be indexed with the (001) and (002) planes, but these peaks are not particularly sharp. The much sharper and stronger peaks in these two scans are due to the substrate, including “ghost” reflections caused by extra radiation lines from the x-ray tube. No possible match to any vanadium oxide was found for the broad 15.7° peak, which could be caused by a poorly crystalized lower oxide. The peak near 38° is caused by silver residue on the sides of the sample, which may remain after the back of the sample is cleaned. The X-ray diffraction results for the two samples grown on STO indicate that in fact VO<sub>2</sub> (B) may be grown on this substrate, but off-plane orientation and phase purity is no better than obtained for the samples grown on glass. Likely, somewhat different growth conditions may improve these results. However, because of the high cost of STO substrates this possibility was not pursued.

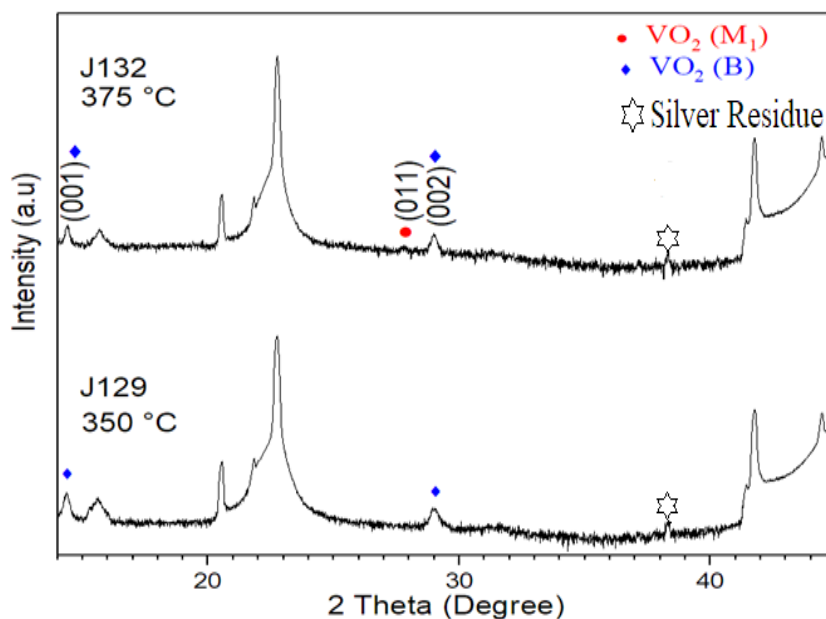


**Figure 5.3:** X-ray diffraction pattern for VO<sub>2</sub> grown over STO substrate at two different temperatures.

Having established the results previously discussed, O<sub>2</sub> flow was decreased from 12.5 to 11.5 sccm for a new set of samples grown on glass substrates. Figure 5.4 presents the diffraction pattern for resulting samples with nearly pure VO<sub>2</sub> (B) -(001) orientation. Average grain size is approximately 41 nm. Sample J165 was grown at 375 °C and, in contrast with sample J127, VO<sub>2</sub> (M<sub>1</sub>) phase is not present. In addition, compared to the background, sample J165 peaks show higher intensities.

VO<sub>2</sub> (B) samples grown at 11.5 sccm oxygen flow rate display strong preferential crystallization in the (00 $l$ ) direction. Although films with 12.5 sccm oxygen flow exhibit the same preference, off-plane orientations are observed. Moreover, maintaining a constant deposition temperature of 375 °C, a 12.5 sccm oxygen flow allowed formation of the VO<sub>2</sub> (M<sub>1</sub>) phase. Instead, VO<sub>2</sub> (B) phase is favoured with a 11.5 sccm oxygen flow rate. Based on these observations, it seems possible to grow highly oriented VO<sub>2</sub> (B) at higher temperatures by lowering the oxygen flow rate. The higher growth temperature is expected to favour enhanced crystallization, which is indicated by the improved orientation.

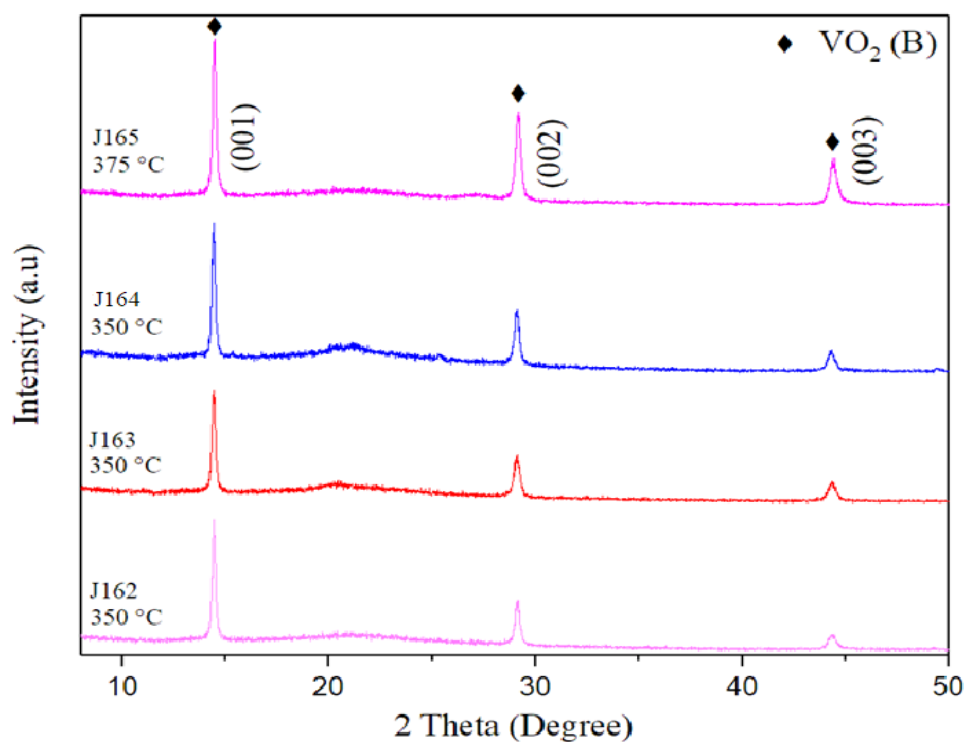


**Figure 5.4:** X-ray diffraction for samples grown at different temperatures under 11.5 sccm oxygen flow rate, in contrast with previous samples.

VO<sub>2</sub> (B) peaks for most samples in table 1 are shifted to higher angles with respect to JCPDS cards for powder diffraction pattern, as seen in figure 5.5 (a)-(b). This can be caused by the differences in lattice parameters and thermal expansion coefficients between the film and the substrates. We consider first the lattice mismatch.

Lattice mismatch between the VO<sub>2</sub> (B) film and STO substrate can be estimated from their lattice constants (bulk values),

$$f = \frac{a_{substrate} - a_{film}}{a_{substrate}} \times 100 \quad (5.1)$$

where  $f$  is the lattice mismatch percentage value. Previous reports have communicated an epitaxial match between STO and VO<sub>2</sub> (B).<sup>57</sup> Lattice mismatch between the substrate and the film must be examined as follows. X-ray diffraction showed VO<sub>2</sub> (B) has a  $(00l)$  preference orientation. This implies planes  $a$  and  $b$  of the film are parallel to the substrate and  $c$  is perpendicular to the substrate's surface. Moreover, VO<sub>2</sub> (B) has a monoclinic structure (in comparison with the STO substrate, which has a cubic structure). Two lattice mismatches are to be considered: between  $a_{VO_2(B)}|a_{STO}$  and between  $b_{VO_2(B)}|a_{STO}$ , and it can be calculated using the values of  $a_{VO_2(B)} = 12.03 \text{ \AA} \approx 3a_{STO} = 11.715 \text{ \AA}$ , and  $b_{VO_2(B)} = 3.69 \text{ \AA} \approx a_{STO} = 3.905 \text{ \AA}$ .<sup>57</sup> The lattice mismatch  $f$  is -2.7% for  $[010]VO_2(B) \parallel [010]STO$  and +5.5% for  $[100]VO_2(B) \parallel [100]STO$ . Negative and positive sign represent compressive and tensile strain, respectively. Since the observed shift of the X-ray diffraction peaks are to higher angles, tensile strain may dominate over the compressive strain. As tensile strain is applied,  $d$  spacing contracts, shifting X-ray peaks to the right in the scan. The previous analysis disregards any strain change which might be introduced by the different thermal contractions of film and substrate after deposition.

Consideration of lattice mismatch is irrelevant for the SiO<sub>2</sub> substrate since it is amorphous and lacks the long-range order that is characteristic of a crystalline substrate. However, even

in this case film strain can be introduced by the difference in thermal expansion coefficients between film and substrate. Upon cooling, substrate and thin film will shrink by some factor given by their respective thermal expansion coefficients  $\alpha$ ,

$$\alpha = \frac{L(T) - L_0}{L_0 \cdot \Delta T} \quad (5.2)$$

where  $L_0$  is the length at the reference temperature (usually room temperature). It follows that two different materials with an  $\alpha_{film}$  and  $\alpha_{substrate}$ , having the same length  $L_0$  at some  $T_0$  will differ in length at a temperature  $T$  by some  $L(T)$ . This will be directly proportional to the mismatch in the thermal expansion coefficient given by,

$$\Delta L_{film}(T) = L_0 \cdot \Delta T \cdot \alpha_{film} \quad (5.3)$$

$$\Delta L_{substrate}(T) = L_0 \cdot \Delta T \cdot \alpha_{substrate} \quad (5.4)$$

The thermal expansion coefficient of  $\text{SiO}_2$  is  $0.5 \times 10^{-6} \text{ K}^{-1}$ .<sup>58</sup> To our knowledge, there is no published data for the  $\text{VO}_2$  (B) thermal expansion coefficient value. Considering the shift to higher angles, it is suggested that the thermal expansion coefficient for  $\text{VO}_2$  (B) is larger than that for the  $\text{SiO}_2$  substrate. As sample temperature starts to decrease after deposition, the film would shrink faster than the substrate, leaving the film in tensile stress. This interpretation seems reasonable since, in general, known expansion coefficients for other  $\text{VO}_2$  phases are higher than for  $\text{SiO}_2$  glass.

For the STO substrate, the thermal expansion coefficient value is  $32.3 \times 10^{-6} \text{ K}^{-1}$ .<sup>59</sup> The peak shift to higher angles would entail the thermal expansion coefficient of the B-phase to be larger than for STO. However, previous studies on  $\text{VO}_2$  (B) deposited over MgO substrate, which has a thermal expansion coefficient of  $13.5 \times 10^{-6} \text{ K}^{-1}$ , has displayed a peak shift to lower angles.<sup>29</sup> This suggests the thermal expansion coefficient of  $\text{VO}_2$  (B) is lower than that for MgO. Considering the results, the difference in thermal expansion coefficient between B-phase  $\text{VO}_2$  and STO does not explain the shift to higher angles.

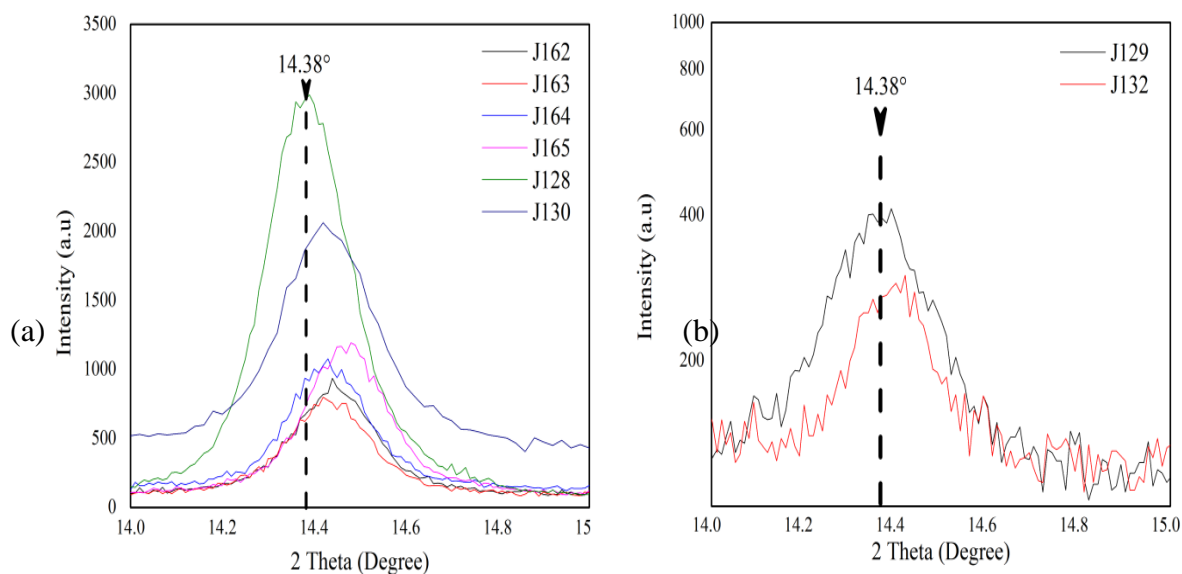


**Figure 5.5:** (a) VO<sub>2</sub>(B) films deposited over SiO<sub>2</sub> substrates and (b) STO substrates. Compared with powder X-ray diffractions, peaks of VO<sub>2</sub>(B) films are shifted to higher angles.

## 5.2 Electrical Characterization

Samples were submitted to a heating cycle ranging from ambient to 400 K while measuring resistivity ( $\rho$ ) as a function of temperature. VO<sub>2</sub>(B) does not present a phase transition unless heated to temperatures as high as 550 °C. As mentioned before, at this temperature, VO<sub>2</sub>(B) transforms to the more stable R phase in what has been found to be an irreversible transformation.<sup>26</sup> Therefore, the samples were tested only up to 400 K (127 °C). A cooling cycle from 300 K to 120 K was performed for the best sample based on the XRD results, in order to explore the electrical characteristics at lower temperatures as well.

Sample J128, grown over SiO<sub>2</sub> substrate, was subjected to a cooling cycle. As seen in figure 5.6 inset, the VO<sub>2</sub>(B) film exhibits a change of ~6 orders of magnitude (0.02 to  $3 \times 10^4$   $\Omega$ -cm) in resistivity while cooling from 300 to 120 K. Also, the conductivity ( $\sigma$ ) curve agrees with reported values for VO<sub>2</sub>(B) thin films over SiO<sub>2</sub> substrates.<sup>29</sup> The change in conductivities from ambient to ~180 K corresponds to a gradual phase transition VO<sub>2</sub>(B) exhibits at low temperatures, as first reported by Oka *et al.*<sup>25</sup> Each of the two phases present a different monoclinic structure (but same space group C2/m). The phase above 300 K and below 300 K

are designated as the high-temperature phase (HTP) and the low-temperature phase (LTP). Conductivity starts to decrease as soon as temperature drops. No hysteresis is observed, compared with the small hysteresis reported in pressed pellets and, in some cases, thin films of VO<sub>2</sub> (B).<sup>30, 60</sup> Moreover, sample J128 presents higher conductivity values, over approximately 3 orders of magnitude, compared to those shown by Rúa *et. al.*<sup>29</sup> Previous authors prepared thin films over glass substrate at 425 °C and attributed the lower conductivity values to the presence of other phases, particularly VO<sub>2</sub> (A). Finally, conductivity increases with increasing temperature (from 120 to 300 K). This behaviour is distinctive in semiconductors.

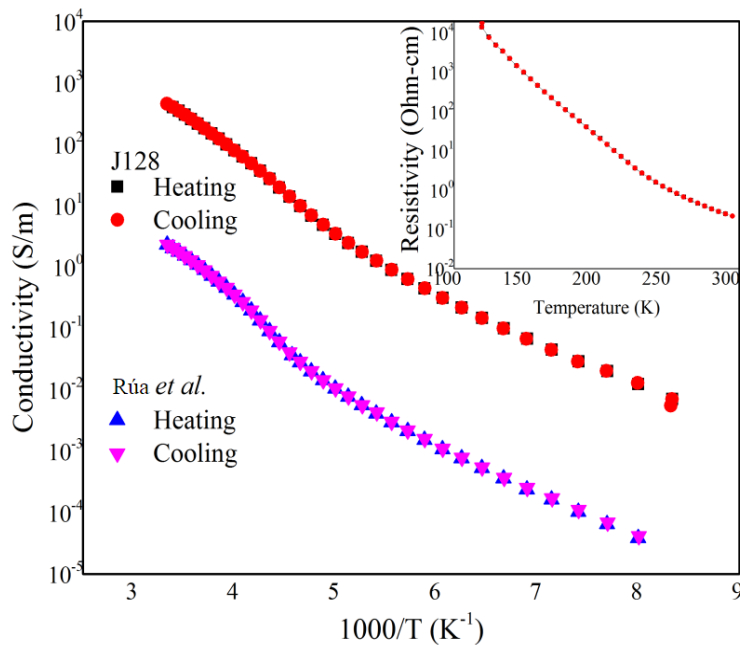


**Figure 5.6:** Arrhenius-type plot of the electrical conductivity for sample J128; inset: resistivity as a function of temperature. No hysteresis is observed from 300 to 120 K.

Electrical conduction in VO<sub>2</sub> (B) cannot be explained using the band model which is successful for common semiconductors. In addition, the present case is further complicated by the fact that films are polycrystalline. Still, plotting  $\ln(\sigma)$  as a function of inverse temperature results in a linear behaviour for  $T \gtrsim 150$  K, revealing that the system must overcome an energy barrier in order for the conductivity to increase (as  $T$  increases). This is known as a thermally activated process which is described by the Arrhenius equation,

$$\sigma = \sigma_0 e^{\left(\frac{-E_a}{kT}\right)} \quad (5.5)$$

where  $\sigma$  is the conductivity,  $\sigma_0$  is a constant independent of  $T$ ,  $k$  is Boltzmann's constant ( $8.6 \times 10^{-5} \frac{eV}{K}$ ),  $T$  is the absolute temperature at which the process occurs and  $E_a$  is the activation energy.

$E_a$  is then estimated from the slope of the linear fitting of  $\ln(\sigma)$  versus  $(\frac{1}{T})$ .

$$m = \frac{-E_a}{k} \quad (5.6)$$

From figure 5.7, the calculated activation energy is 137 meV. Compared to the 139 meV previously reported over glass substrates,<sup>26</sup> it is in very good agreement.

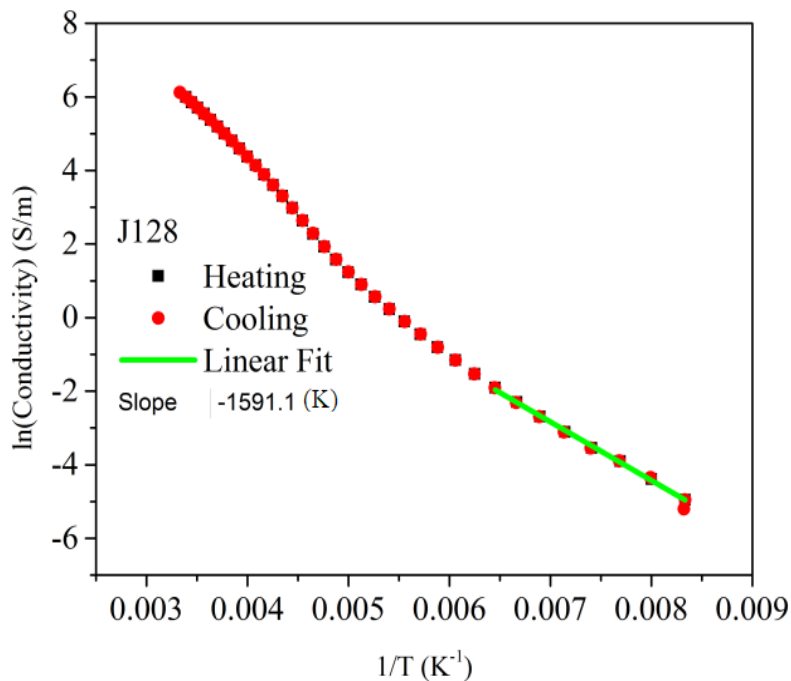


**Figure 5.7:** Arrhenius behaviour is observed with  $\ln(\sigma)$  as a function of  $1/T$  for  $T \gtrsim 150$  K.

All samples were submitted to resistivity measurements at high temperatures. Samples J131 and J164 displayed results which are inconsistent with those of other samples, possibly because of admixture of phases, and are not presented in this work.

Figure 5.8 shows resistivity as a function of temperature for samples J127 and J130. Recalling figure 5.2, X-ray diffraction displays  $VO_2$  ( $M_1$ ) phase in sample J127 as growth temperature was raised to 375 °C under 12.5 sccm oxygen flow. Indeed, figure 5.8 (a) displays a resistivity vs. temperature response consistent with  $VO_2$  ( $M_1$ ). Figure 5.8 (b) corresponds to

sample J130 which, based on the X-ray diffraction results, exhibits single-phase VO<sub>2</sub> (B). The resistivity curve decreases continuously as the film is heated from ambient to 400 K. At room temperature, sample J130 displays a value of 0.16 Ohm-cm, compared to the 0.02 Ohm-cm reported by Lee *et. al.*<sup>57</sup>

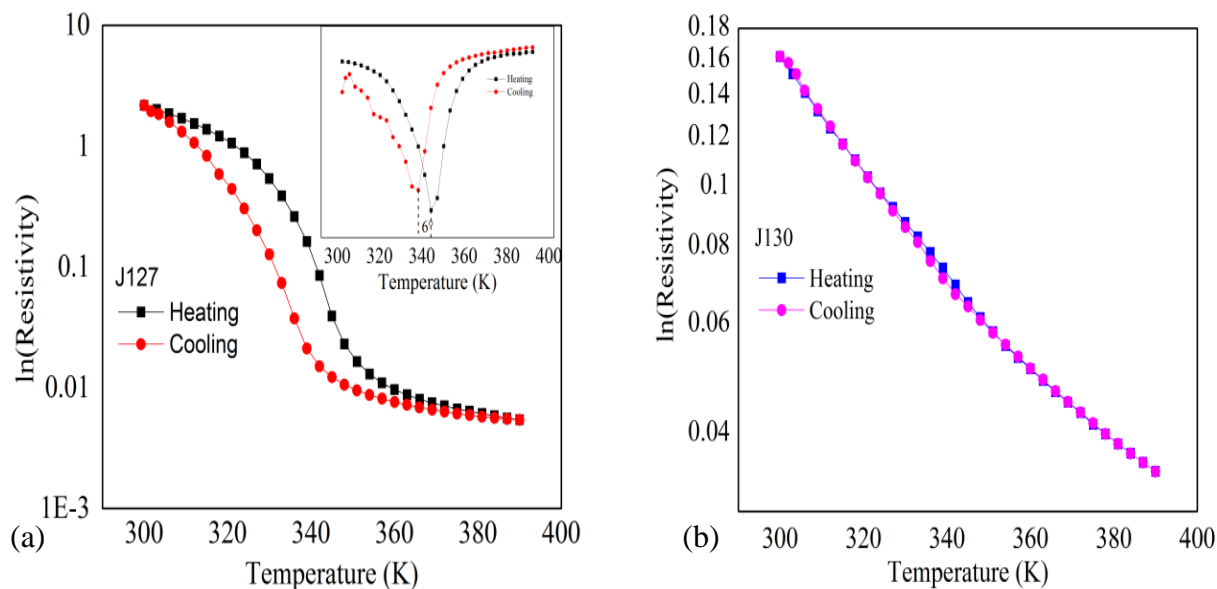


**Figure 5.8:**  $\ln(\text{Resistivity})$  as a function of temperature for samples (a) J127 and (b) J130.

On closer inspection of the behaviour of VO<sub>2</sub> (B) resistivity at higher temperatures, the response is not truly linear, as a change in slope is observed at  $\sim 68$  °C and  $\sim 64$  °C on heating and cooling, respectively, for sample J128 as seen in figure 5.9 (a)-(b). Figure 5.9 (c)-(d) shows sample J130 exhibits also a change of slope but is shifted to a higher temperature. It can be safely assumed that samples J128 and J130 possess a small concentration of M<sub>1</sub> undergoing phase transition, although not observed in the diffraction patterns.<sup>61-63</sup>

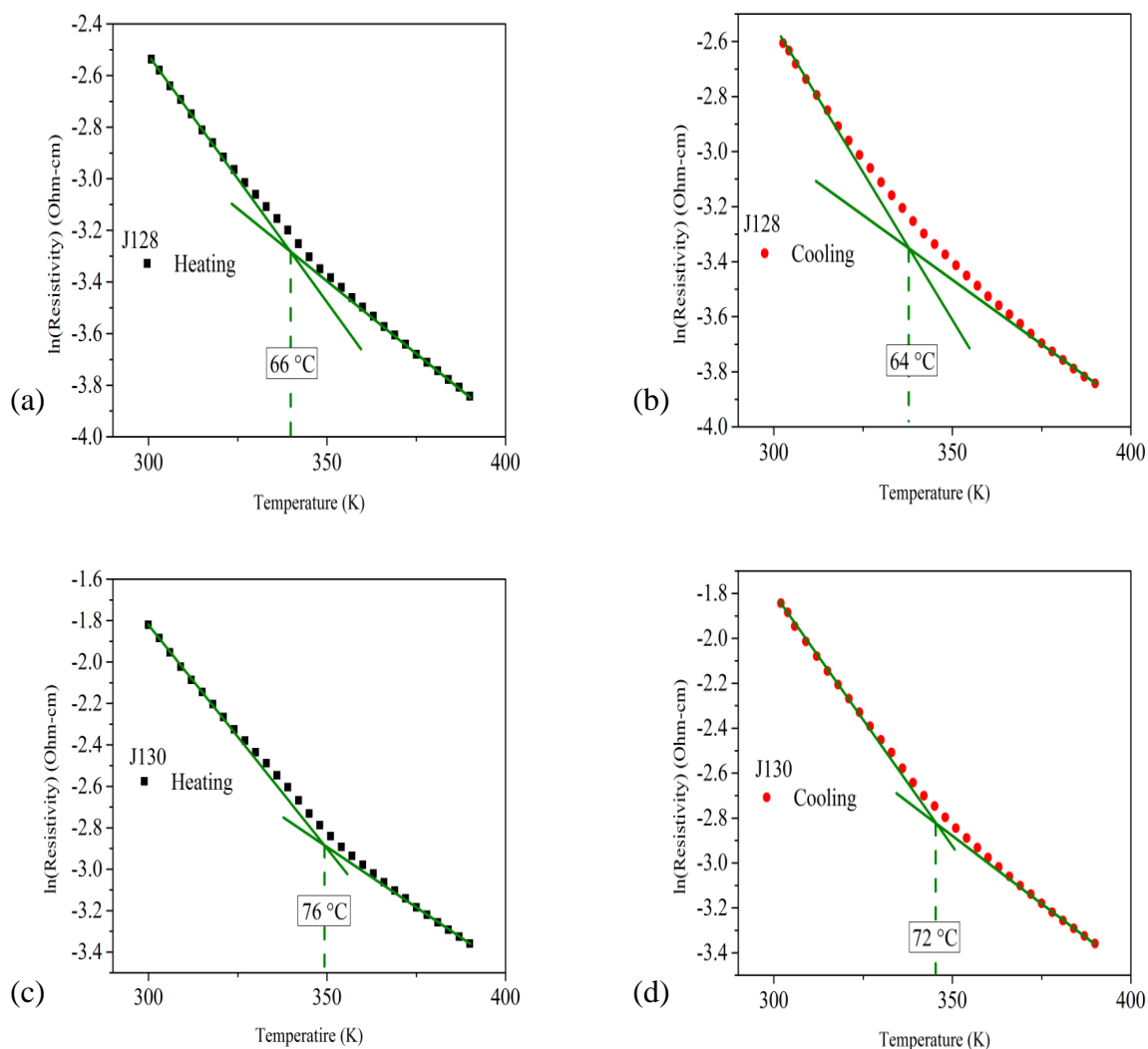


**Figure 5.9:**  $\ln(\text{Resistivity})$  as a function of temperature displays a change of slope for (a)-(b) sample J128 and (c)-(d) sample J130.

The change was also observed on samples J162, J163 and J165, prepared with 11.5 sccm oxygen flow, as seen in figure 5.10 (a)-(f). Nevertheless, a shift to higher temperatures for the change of slope is perceptible. This may be associated with deviation from correct stoichiometry for  $\text{VO}_2$ . While stoichiometric  $\text{VO}_2$  has transition temperature (on heating) at  $\sim 68^\circ\text{C}$ , high and low stoichiometric  $\text{VO}_{2 \pm x}$  displays the transition at higher and lower temperatures respectively.<sup>64, 65</sup> Also, having lower oxygen partial pressure does not necessarily leads to oxygen deficiency.<sup>66</sup> Based on these observations, it can be argued that samples prepared with 11.5 sccm have a small concentration of  $\text{VO}_2$  ( $M_1$ ) with higher oxidation composition (positive  $x$ ).

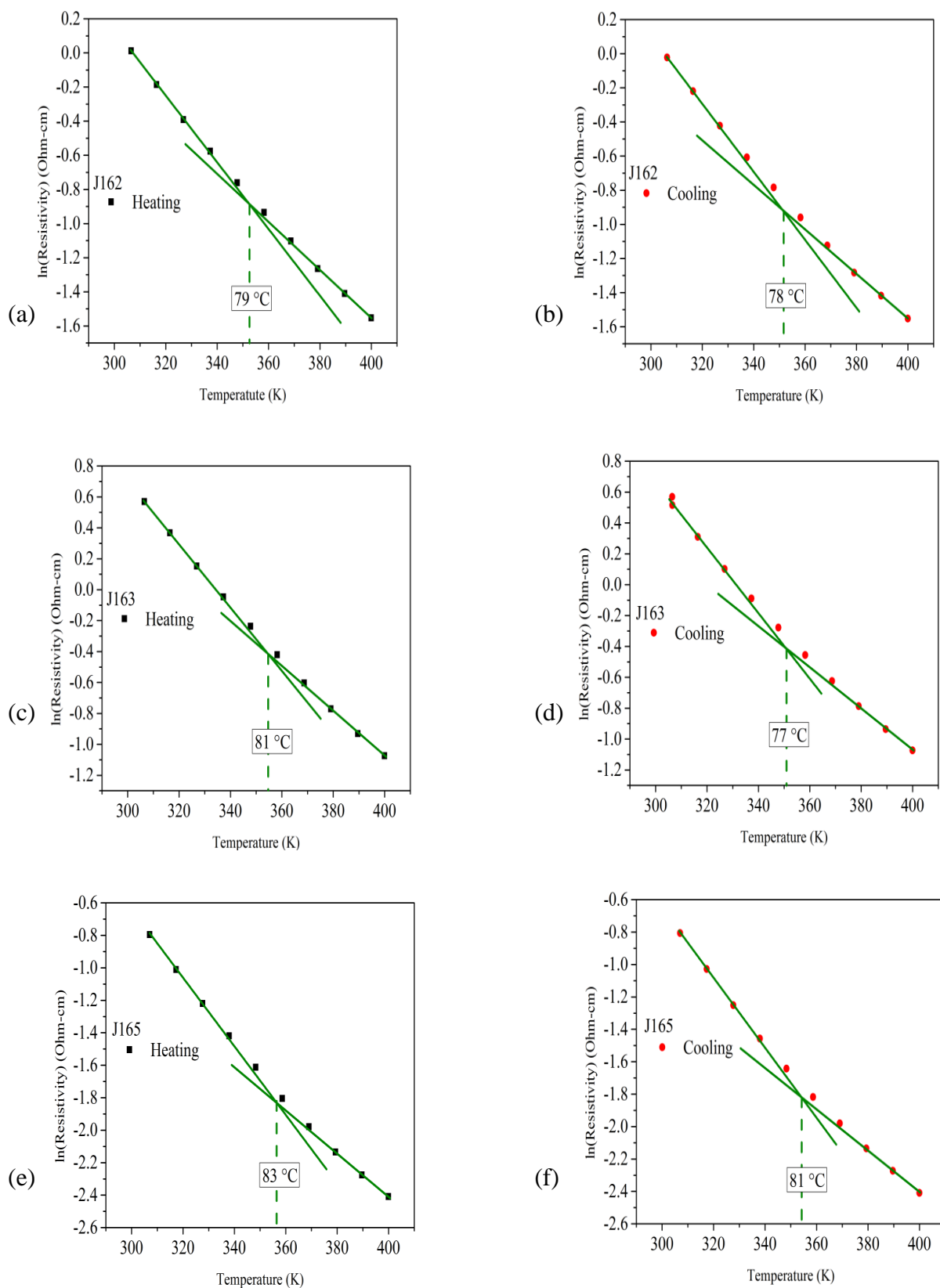


**Figure 5.10:**  $\ln(\text{Resistivity})$  as a function of temperature displays a change of slope to higher temperatures for (a)-(b) sample J162, (c)-(d) sample J163 and (e)-(f) sample J165. Higher temperature shift is attributed to deviation from stoichiometry for  $\text{VO}_2$  ( $M_1$ ).

All previous samples (except J127 and J132) contain a small concentration of  $M_1$  phase, despite the fact X-ray diffraction did not show any peaks. Slope values were calculated before (left slope) and after (right slope) the transition for heating and cooling cycles, as seen in table 5.3. The average slope value before and after the transition is  $-0.02 \text{ Ohm} - \text{cm}/\text{K}$  and  $-0.01 \text{ Ohm} - \text{cm}/\text{K}$ , respectively.

Sample	Heating Cycle Left Slope ( $\text{Ohm} - \text{cm}/\text{K}$ )	Heating Cycle Right Slope ( $\text{Ohm} - \text{cm}/\text{K}$ )	Cooling Cycle Left Slope ( $\text{Ohm} - \text{cm}/\text{K}$ )	Cooling Cycle Right Slope ( $\text{Ohm} - \text{cm}/\text{K}$ )
J128	-0.019	-0.010	-0.020	-0.019
J130	-0.022	-0.011	-0.024	-0.011
J162	-0.019	-0.013	-0.019	-0.012
J163	-0.020	-0.014	-0.021	-0.013
J165	-0.020	-0.013	-0.021	-0.013
<b>Average</b>	<b>-0.020</b>	<b>-0.012</b>	<b>-0.021</b>	<b>-0.014</b>

**Table 5.3:** Slope values for various samples. A change of  $-0.01 \text{ Ohm} - \text{cm}/\text{K}$  is observed which is attributed to the small concentration of  $M_1$  phase mixed with  $\text{VO}_2$  (B) films.

Samples J129 and J132 were deposited over STO substrate. Recalling figure 5.3, sample J129 did not display any X-ray diffraction peaks corresponding to  $\text{VO}_2$  ( $M_1$ ). Yet the resistivity curve exhibits a small hysteresis and slope change near the temperature range characteristic of ( $M_1$ ) phase, as seen in figure 5.11 (a). Considering all results, none of the films produced are single-phase  $\text{VO}_2$  (B) but contain at least a small admixture of  $\text{VO}_2$  ( $M_1$ ).

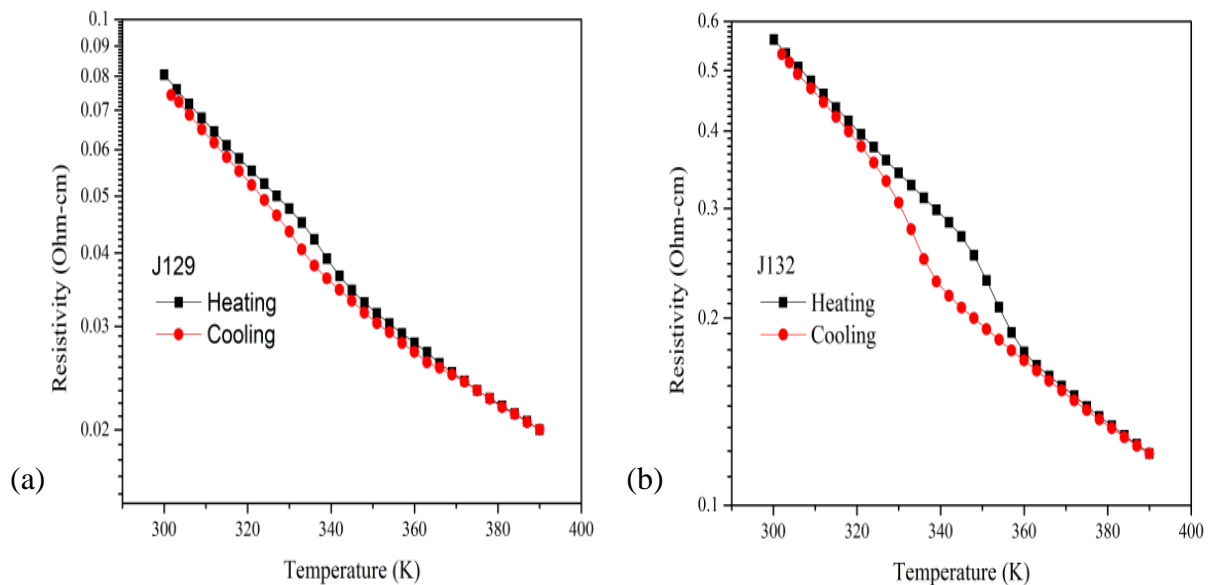


**Figure 5.11:** Resistivity vs. temperature for  $\text{VO}_2$  (B) thin films grown over STO substrate. Characteristic hysteresis behaviour of the  $M_1$  phase undergoing transition is observed in sample (a) J129 and (b) J132.

Recent investigations show the potential of VO<sub>2</sub> (B) in Li-ion batteries although having a low conductivity issue. It has been argued that with a small admixture of the M phase it presents a promising alternative solution.<sup>56, 67-69</sup>

For a small temperature range, the variation can be represented as a linear relation,

$$R = R_{Ref}[1 + \alpha(T - T_{Ref})] \quad (5.7)$$

where  $R$  is the conductor's resistance at temperature  $T$ ,  $R_{Ref}$  is the conductor's resistance at room temperature  $T_{Ref}$ , and  $\alpha$  is the temperature coefficient of resistance (TCR) for the conductor material. Most materials change specific resistance with changes in temperature, which is why figures of specific resistance are always specified at a standard temperature. For sample J128, the TCR is calculated as follows,

$$\alpha = \frac{\ln(\text{Resistivity})}{\text{Temperature}} \times 100 \quad (5.8)$$

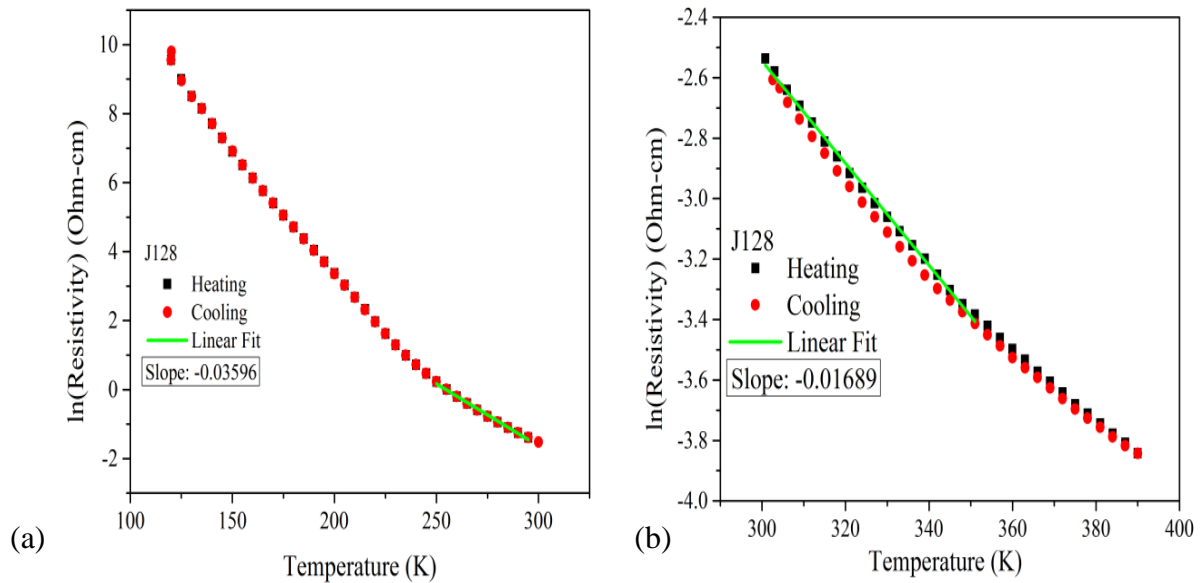


**Figure 5.12:** (a) Linear fit for 250-300 K temperature range and (b) linear fit for 300-350 K temperature range for sample J128.

From figure 5.12, the TCR between 300 K and 250 K is  $-3.6\% \text{ K}^{-1}$  in exact agreement with the value previously reported by Rúa et al.<sup>29</sup> The TCR between 300 K and 350 K is  $-1.7 \text{ K}^{-1}$ . Resistivity measurements on cooling and heating cycles were done with different equipment, but this is not thought to have affected this result. Instead, it should be recalled that the

transition from the low-temperature to the high-temperature phase in VO<sub>2</sub> (B) is completed at approximately room temperature.

### 5.3 Atomic Force Microscope (AFM) Analysis

The surfaces of two VO<sub>2</sub> (B) samples deposited on glass were analysed by atomic force microscopy (AFM). Table 5.4 presents the results for surface roughness, height distribution and average lateral grain size.

Sample	RMS Surface Roughness(nm)	Surface Height Distribution (nm)	Average Lateral grain size (nm)
J162	10	38	121
J165	13	34	158

**Table 5.4:** AFM vertical and lateral grain size for samples J162 and J165.

Figure 5.13 show 5 x 5 μm and 1 x 1 μm AFM images for sample J162 and figure 5.14 show 3 x 3 μm and 1 x 1 μm AFM images for sample J165. Average (rms) surface height distribution values of 38 and 34 nm, respectively, were obtained. To calculate the average lateral grain size of the samples, Heyn's technique was employed.<sup>70</sup> A line is drawn over the 1 x 1 μm AFM images. To determine the real length of the line  $l$ , the scale provided by the program on the picture was used. The number of grain boundary intercepts  $n$  is counted. The lateral grain size  $\Lambda$  is determined by

$$\Lambda = \frac{l}{n} \quad (5.9)$$

The measurement was repeated with different line orientations on several fields of view. Averaging the values result in grain sizes of 121 nm for sample J162 and 158 nm for sample J165. As seen in figures 5.13 and 5.14, these grains result in numerous grain boundaries (GB). This imperfection has an impact in the electrical properties and is expected to increase sample resistivity.

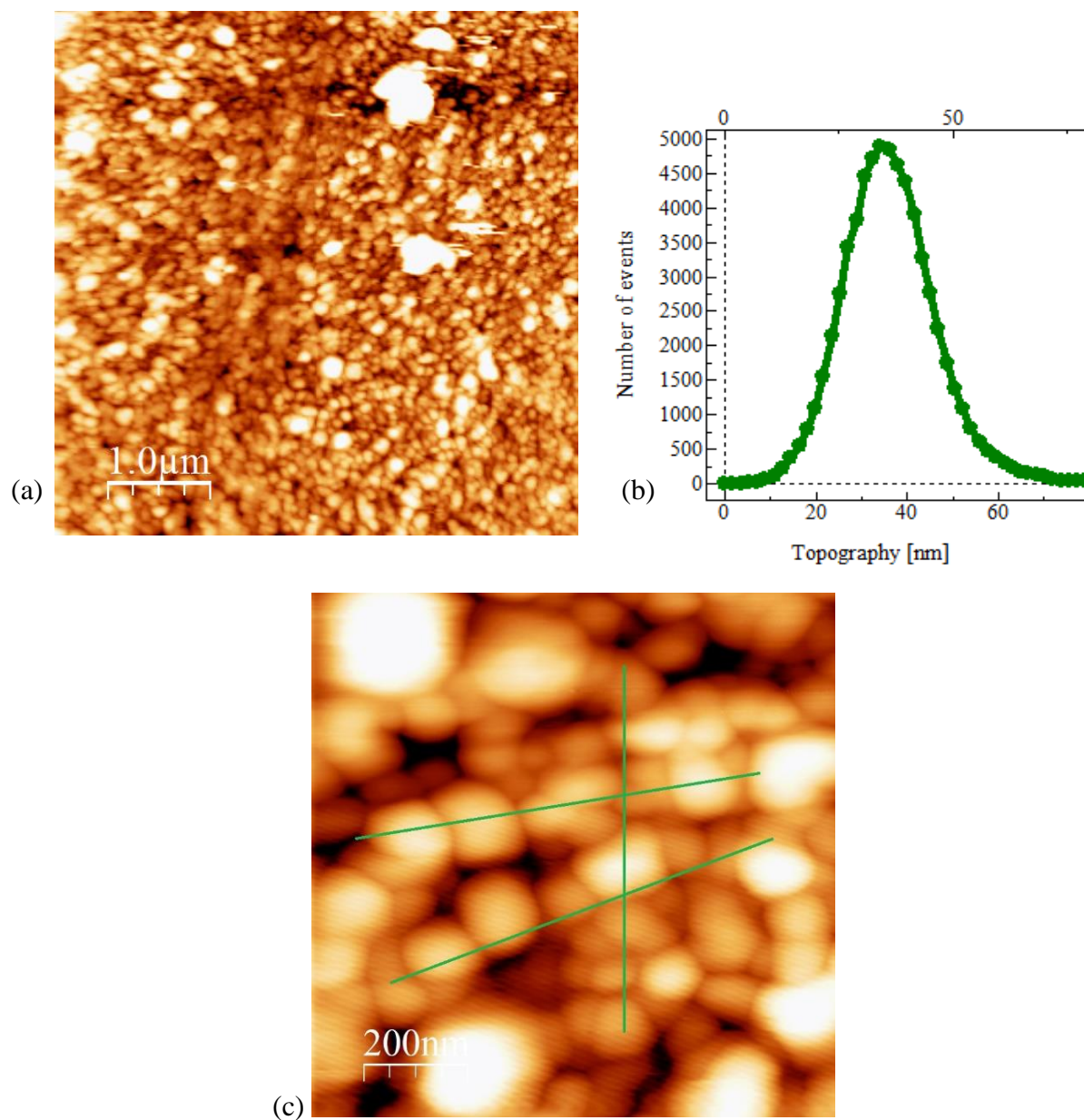


**Figure 5.13:** (a) AFM image for sample J162. (b) Surface height distribution is  $\sim 38$  nm. (c) Average lateral grain size is  $\sim 121$  nm. Images processed using WSxM [71].

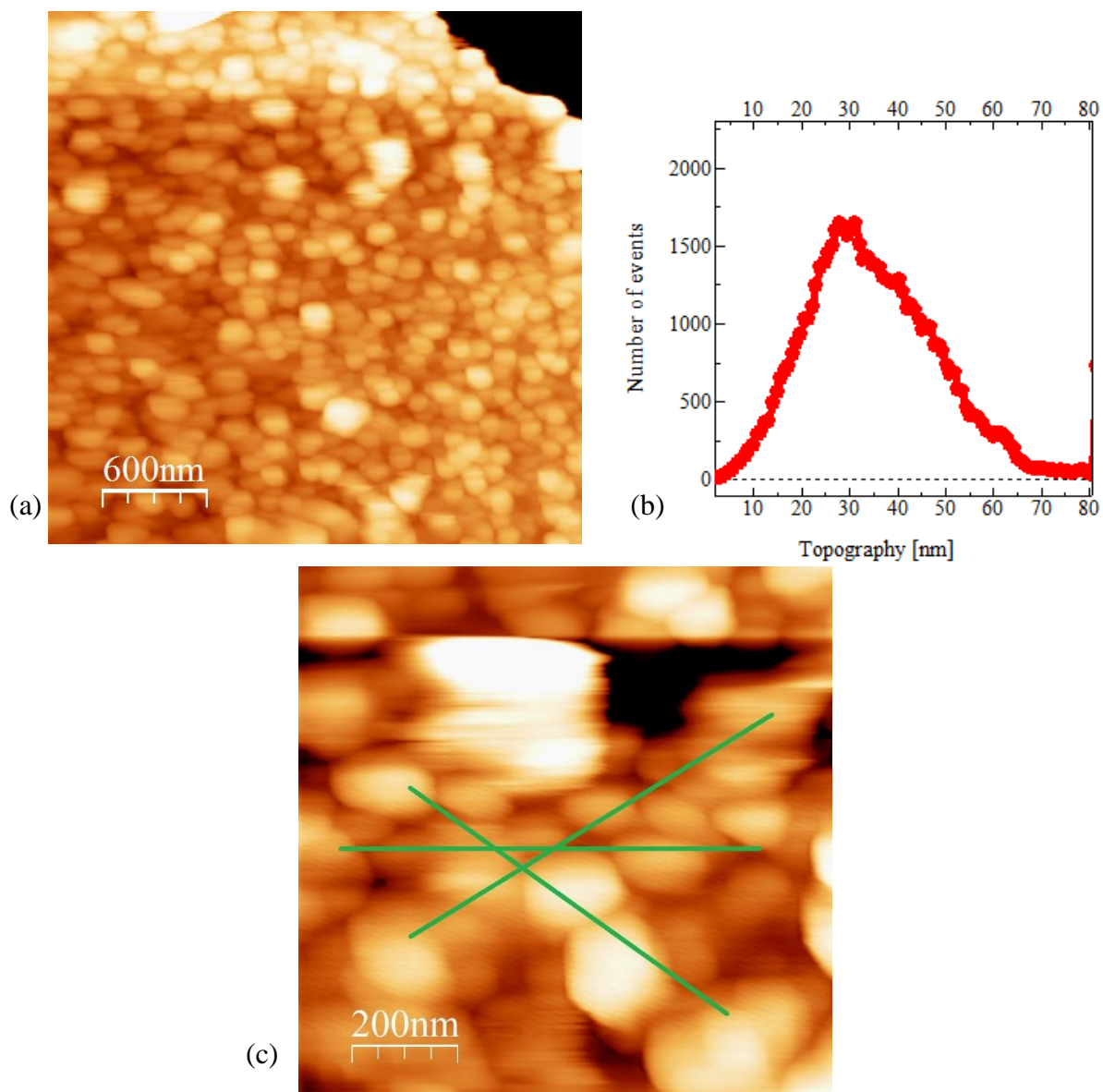


**Figure 5.14:** (a) AFM image for sample J165. (b) Surface height distribution is  $\sim 34$  nm. (c) Average lateral grain size is  $\sim 158$  nm. Images processed using WSxM [71].

The lattice structure at a grain boundary is distorted. The distortions generate a large number of defects which result in the formation of trapping states.<sup>72</sup> After confining the carriers, traps become electrically charged. This generates a potential barrier that obstructs the mobility of the carriers from one grain to another, hence, affecting the electrical properties of the semiconductor. Recalling figure 5.6, sample J128 displayed higher conductivity values than those reported by Rúa *et. al.*<sup>29</sup> It was determined that a small concentration of VO<sub>2</sub> (M<sub>1</sub>) phase was present in the VO<sub>2</sub> (B) thin films although not necessarily observed in the XRD. Thus, the higher conductivity may be caused by the admixture of the VO<sub>2</sub> (M<sub>1</sub>) phase.

## Chapter 6 Conclusion

Thin films of nearly pure B-phase  $\text{VO}_2$  were successfully produced by pulsed-DC magnetron reactive sputtering technique. The sputtering technique allows many advantages such as high deposition rates, high-purity films and the ability to coat heat-sensitive substrates, ease of sputtering any metal, excellent uniformity and high adhesion of films. However, reactive sputtering suffers from a drawback. As oxygen gas was injected to the chamber, ideally it would combine only with the film growing on the substrate. However, this is not true as it combines also with the target. This leads to compositional change of the target and therefore to process instabilities associated with a hysteresis control loop which can arise, in addition to arcing and disappearing anode. A study of the cathode potential as a function of gas flow was done. The hysteresis displayed at the reactive region was reduced by increasing the argon flow from 25 to 100 sccm, having a vertical width of  $\sim 3$  V. This value in the reactive region implies that the region achieves a much better stabilization and control of film composition should be more easily achieved. Furthermore, this increased flow affected the “metallic” region of the control loop by increasing its range of stability from 0 to 1.2 sccm of oxygen. Although it was demonstrated that Ar working pressure did not play a significant role over the instabilities, a 5 - 6.2 mTorr working pressure was used for film growth. At this pressure ejected atoms from the target can move towards the substrate with few collisions with atoms in the chamber atmosphere and arrive at the growing film with high kinetic energies.

The behaviour of the voltage as a function of the oxygen flow was studied at different sputtering power settings (100, 200 and 300 Watts) at the working pressure range previously mentioned. It was established that an increase in power causes an increase in the range of the “metallic” region in the control loop. Higher power translates to higher number of ions hitting the target per minute. As target material atoms are being sputtered faster, oxidation is prevented resulting in a longer metallic portion of the curve. For growth of  $\text{VO}_2$  (B) thin films a sputtering

power of 200 Watts was chosen. Finally, it was noticed that growth conditions established to produce films with a particular composition would not yield reproducible results after the target had been used for a number of hours. It was found that, as the target became thinner, high voltage values were achieved with lower oxygen flow. A noticeable decrease in the metallic region was observed.

Using optimized deposition parameters, thin films of nearly pure VO<sub>2</sub> (B) were deposited under 12.5 and 11.5 sccm of oxygen flow over SiO<sub>2</sub> and SrTiO<sub>3</sub> substrates. Three distinct XRD peaks at 14.24°, 29.04° and 44.14° were indexed to (00*l*) family planes. Thus, the VO<sub>2</sub> (B) films show strong preferential crystallization orientation over that direction for temperatures of 350 and 375 °C. Peaks were shifted to higher angles with respect to powder diffraction standards, meaning that the films are in tensile stress. For the VO<sub>2</sub> (B)/SrTiO<sub>3</sub> samples, the shift was attributed to the difference in lattice parameters. For the VO<sub>2</sub> (B)/SiO<sub>2</sub> samples, difference in thermal coefficients were responsible for the shift.

The influence of deposition temperature over resulting phase was also investigated. Maintaining a constant oxygen flow of 12.5 sccm, temperature was varied from 375 to 325 °C at intervals of 25 degrees. A peak at 27.78°, which is assigned to VO<sub>2</sub> (M<sub>1</sub>), appeared as the deposition temperature was increased to 375 °C. Electrical measurements confirmed that indeed the M<sub>1</sub> phase was present. Consequently, a difference of just 25 degrees in deposition temperature may determine whether the VO<sub>2</sub> (M<sub>1</sub>) or VO<sub>2</sub> (B) phase is obtained.

Sample J128 exhibited a change of 6 orders in resistivity while cooling from 300 to 120 K. Also, a drop in conductivity with no hysteresis was observed, in agreement with recent studies. The conduction mechanism was difficult to analyse. Nevertheless, plotting  $\ln(\sigma)$  as a function of inverse temperature resulted in a linear behaviour for  $T \gtrsim 150$  K, revealing the system must overcome an energy barrier in order for the conductivity to increase (as  $T$  increases). This thermally activated process was described by an Arrhenius plot in which activation energy was

137 meV. The latter value goes in accord with previously reported over glass substrates. TCR coefficient was -3.6% and -1.7%  $K^{-1}$  for cooling and heating cycles, respectively. It is recalled that the transition from the low to high temperature phase of VO<sub>2</sub> (B) is completed at room temperature.

A detailed analysis for the heating cycle of the samples was done. A change of slope in the resistivity measurements was observed which was attributed to the VO<sub>2</sub> (M<sub>1</sub>) concentration on VO<sub>2</sub> (B) thin films. Samples grown at 350 °C displayed a change of slope at ~68 °C. However, samples grown at 375 °C displayed the slope change at ~78 °C. This was attributed to the amount of concentration and the stoichiometry of VO<sub>2</sub> (M<sub>1</sub>). Finally, grain size for VO<sub>2</sub> (B) thin films of samples J162 and J165 were studied. Using Heyn's technique, average lateral grain size was 121 nm for sample J162 and 158 nm for sample J165. Due to the small VO<sub>2</sub> (B) grain size, it results in more grain boundaries which are expected to impact the electrical properties of VO<sub>2</sub> (B), increasing sample resistivity.

## References

- <sup>1</sup>E. Kusano, J.A Theil, J. Thornton. *Deposition of vanadium oxide films by direct-current magnetron reactive sputtering*. Journal of Vacuum Science and Technology A **6**, 1663 (1988).
- <sup>2</sup>L. Jiran, H. Ming, L. Zhigang, H. Lei, C. Tao. *Fabrication and Characterization of VO<sub>2</sub> Thin Films by Direct Current Facing Targets Magnetron Sputtering and Low Temperature Oxidation*. Transactions of Taijin University **14**, 12209 (2008).
- <sup>3</sup>F. Morin. *Oxides which Show a Metal-to-Insulator Transition at the Neel Temperature*. physical Review Letters **3**, 34 (1959).
- <sup>4</sup>B. Allimi, S. Alpay, C. Xie, B. Wells, J. Budnick and D. Pease. *Resistivity of V<sub>2</sub>O<sub>3</sub> thin films deposited on a *a*-plane (110) and *c*-plane (001) sapphire by pulsed laser deposition*. Applied Physics Letters **92**, 202105 (2008).
- <sup>5</sup>N. Bahlawane and D. Lenoble. *Vanadium Oxide Compounds: Structure, Properties, and Growth from the Gas Phase*. Chemical Vapor Deposition **20**, 299 (2014).
- <sup>6</sup>K. Tsai, T. Chin, H. Shien. *Properties of VO<sub>2</sub> Films Sputter-Deposited from V<sub>2</sub>O<sub>5</sub> Target*. Japanese Journal of Applied Physics **42**, 4480 (2003).
- <sup>7</sup>S. Popuri, A. Artemenko, C. Labrugere, M. Miclau, A. Villesuzanne, M. Pollet. *VO<sub>2</sub> (A): Reinvestigation of crystal structure, phase transition and crystal growth mechanism*. Journal of Solid State Chemistry **213**, 79 (2014).
- <sup>8</sup>C. Leroux, G. Nihoul, G. Tendeloo. *From VO<sub>2</sub> (B) to VO<sub>2</sub> (R): Theoretical structures of VO<sub>2</sub> polymorphs and in situ electron microscopy*. Physical Review B **57**, 5111 (1998).
- <sup>9</sup>Virtual NanoLab version 2015.1, QuantumWise A/S.
- <sup>10</sup>T. Reeswinkel, D. Music, J. Schneider. *Ab initio calculations of the structure and mechanical properties of vanadium oxides*. Journal of Physics: Condensed Matter **21**, 145404 (2009).
- <sup>11</sup>J. Feinleib, W. Paul. *Semiconductor-To-Metal Transition in V<sub>2</sub>O<sub>3</sub>*. Physical Review **155**, 841 (1967).
- <sup>12</sup>P. D. Dernier and M. Marezio. *Crystal Structure of the Low-Temperature Antiferromagnetic Phase of V<sub>2</sub>O<sub>3</sub>*. Physical Review B **2**, 3771 (1970).
- <sup>13</sup>R. E. Word, S. A. Werner, W. B. Yelon, J. M. Honig, S. Shivashankar. *Spin waves in vanadium sesquioxide V<sub>2</sub>O<sub>3</sub>*. Physical Review B **23**, 3533 (1981).
- <sup>14</sup>M. Foëx. *Étude dilatométrique et électrique de l'anomalie, présentée à basse température, par le sesquioxyde de vanadium*. Académie des Sciences **23**, 1126 (1946).
- <sup>15</sup>F. J. Morin. *Oxides of the 3d Transition Metals*. The Bell System Technical Journal **37**, 1047 (1958).

- <sup>16</sup>E. N. Fuls, D. H. Hensler and A. R. Ross. *Reactively Sputtered Vanadium Dioxide Thin Films*. Applied Physics Letters **10**, 199 (1967).
- <sup>17</sup>G. A. Rozgonyi and D. H. Hensler. *Structural and Electrical Properties of Vanadium Dioxide Thin Films*. Journal of Vacuum Science and Technology **5**, 194 (1968).
- <sup>18</sup>E. E. Chain. *The influence of deposition temperature on the structure and optical properties of vanadium oxide films*. Journal of Vacuum Science and Technology A. **4**, 432 (1986).
- <sup>19</sup>K. Y. Tsai and T. Chin. *Effects of as-deposited residual stress on transition temperatures of VO<sub>2</sub> thin films*. Journal of Materials Research **19**, 2306 (2004).
- <sup>20</sup>A. Rúa, F. Fernández and N. Sepulveda. *Bending in VO<sub>2</sub>-coated microcantilevers suitable for thermally activated actuators*. Journal of Applied Physics **107**, 074506 (2010).
- <sup>21</sup>F. Théobald, R. Cabala and J. Bernard. *Essai sur la Structure de VO<sub>2</sub> (B)*. Journal of Solid State Chemistry **17**, 431 (1976).
- <sup>22</sup>W. Brückner. *Structural Relations between the VO<sub>2</sub> Phases*. Crystal Research and Technology **16**, K28 (1981).
- <sup>23</sup>Y. Oka, T. Yao and N. Yamamoto. *Powder X-Ray Crystal Structure of VO<sub>2</sub> (A)*. Journal of Solid State Chemistry **86**, 116 (1990).
- <sup>24</sup>Y. Oka, T. Yao and N. Yamamoto. *Structural Phase Transition of VO<sub>2</sub> (B) to VO<sub>2</sub> (A)*. Journal of Materials Chemistry **1**, 815 (1991).
- <sup>25</sup>Y. Oka, T. Yao and N. Yamamoto. *Phase Transition and V<sup>4+</sup>-V<sup>4+</sup> Pairing in VO<sub>2</sub> (B)*. Journal of Solid State Chemistry **105**, 271 (1993).
- <sup>26</sup>J. C. Valmalette and J. R. Gavarri. *High efficiency thermochromic VO<sub>2</sub>(R) resulting from the irreversible transformation of VO<sub>2</sub>(B)*. Material Science and Engineering B. **54**, 168 (1998).
- <sup>27</sup>S. R. Popuri, M. Miclau, A. Artemenko, C. Labrugere, A. Villesuzanne and M. Pollet. *Rapid Hydrothermal Synthesis of VO<sub>2</sub> (B) and Its Conversion to Thermochromic VO<sub>2</sub> (M<sub>1</sub>)*. Inorganic Chemistry. **52**, 4780 (2013).
- <sup>28</sup>S. Chen, J. Lai, J. Dai, H. Ma, H. Wang and X. Yi. *Characterization of nanostructured VO<sub>2</sub> thin films grown by magnetron controlled sputtering deposition and post annealing method*. Optics Express. **17**, 24153 (2009).
- <sup>29</sup>A. Rúa, R. Díaz, S. Lysenko and F. Fernández. *Semiconductor-insulator transition in VO<sub>2</sub> (B) thin films grown by pulsed laser deposition*. Journal of Applied Physics. **118**, 125308 (2015).
- <sup>30</sup>A. Srivastava, H. Rotella, S. Saha, B. Pal, G. Kalon, S. Mathew, M. Motapothula, M. Dykas, P. Yang, E. Okunishi, D. Sarma and T. Venkatesan. *Selective growth of single phase VO<sub>2</sub> (A, B, and M) polymorph thin films*. Applied Physics Letter. **3**, 026101 (2015).
- <sup>31</sup>S. Swann. *Magnetron Sputtering*. Physics in Technology **19**, 67 (1988).

- <sup>32</sup>D. Carter, G. McDonough and D. Christie. *Target Utilization in Pulsed-dc Sputtering Processes*, in Proceedings of the Annual Technical Conference Society of Vacuum Coaters, Colorado, 2007.
- <sup>33</sup>S. Schiller, K. Goedicke, J. Reschke, V. Kirchhoff, S. Schneider and F. Milde. *Pulsed magnetron sputter technology*. Surface and Coating Technology **61**, 331 (1993).
- <sup>34</sup>A. Belkind, Z. Zhao, D. Carter, L. Mahoney, G. McDonough, G. Roche, G. Scholl and H. Walde, *Pulsed-DC Reactive Sputtering of Dielectrics: Pulsing Parameter Effects*, in Proceedings of the Annual Technical Conference -Society of Vacuum Coaters, Denver, 2000.
- <sup>35</sup>A. Spencer, R. Howson and R. Lewin. *Pressure Stability in Reactive Magnetron Sputtering*. Thin Solid Films **158**, 141 (1988).
- <sup>36</sup>S. Berg, H. Blom, T. Larsson and C. Nender. *Modeling of Reactive Sputtering of Compound Materials*. Journal of Vacuum Science and Technology A: Vacuum, Surfaces and Films **5**, 202 (1987).
- <sup>37</sup>S. Kadlec, J. Musil and H. Vyskocil. *Hysteresis Effect in Reactive Sputtering: A Problem of System Stability*. Journal of Physics D: Applied Physics **19**, 187 (1986).
- <sup>38</sup>C. Li, J. Hsieh. *Stability Analysis of Reactive Sputtering Process*. Surface and Coatings Technology **117**, 824 (2004).
- <sup>39</sup>S. Berg and T. Nyberg. *Fundamental Understanding and Modeling of Reactive Sputtering Processes*. Thin Solid Films **476**, 215 (2005).
- <sup>40</sup>E. Särhammar, K. Strijckmans, T. Nyberg, S. Van Steenberge, S. Berg and D. Depla. *A Study of the Process Pressure Influence in Reactive Sputtering Aiming at Hysteresis Elimination*. Surface and Coatings Technology **232**, 357 (2013).
- <sup>41</sup>A. Anders. *Physics of arcing, and implications to sputter deposition*. Thin Solid Films **502**, 22 (2004).
- <sup>42</sup>D. Christie, *Dual Magnetron Sputtering: More than meets the eye*. Society of Vacuum Coaters Bulletin, Fall 2013, Pag. 34.
- <sup>43</sup>E. Shidoji, M. Nemoto, T. Nomura and Y. Yoshikawa. *Three-Dimensional Simulation of Target Erosion in DC Magnetron Sputtering*. Japanese Journal of Applied Physics **33**, 4281 (1994).
- <sup>44</sup>Q. Qiu, Q. Li, J. Su, Y. Jiao and J. Finley. *Influence of Operating Parameters on Target Erosion of Rectangular Planar DC Magnetron*. IEEE Transactions on Plasma Science **36**, 1899 (2008).
- <sup>45</sup>M. Elliot Schoff. (2009). *Sputter Target Erosion and its Effects on Long Duration DC Magnetron Sputter Coating* (Thesis). UC San Diego: b6289911. Retrieved from: <http://escholarship.org/uc/item/8fr0n3g6>

- <sup>46</sup>APD Cryogenics Inc, Cryopump Model APD-8SC Technical Manual, Revision E ed., Allentown, PA: APD Cryogenics, 1995, pp. 7-8.
- <sup>47</sup>J. Andújar, E. Bertran, A. Canillas, C. Rocha and J. Morenza. *Influence of pressure and radio frequency power on deposition rate and structural properties of hydrogenated amorphous silicon thin films prepared by plasma deposition*. Journal of Vacuum Science Technology A **9**, 2216 (1991).
- <sup>48</sup>J. Theil, E. Kusano and A. Rockett. *Vanadium reactive magnetron sputtering in mixed Ar/O<sub>2</sub> discharges*. Thin Solid Films **298**, 122 (1997).
- <sup>49</sup>M. Eckert. *Max von Laue and the discovery of X-ray diffraction in 1912*. Annals of Physics **524**, A83 (2012).
- <sup>50</sup>A. Patterson. *The Scherrer Formula for X-Ray Particles Size Determination*. Physical Review **56**, 978 (1939).
- <sup>51</sup>G. Binning, C. Quate and C. Gerber. *Atomic-Force Microscope*. Physical Review Letters **56**, 930 (1986).
- <sup>52</sup>R. Chwang, B. Smith and C. Crowell. *Contact Size Effects on the Van der Pauw Method for Resistivity and Hall Coefficient Measurement*. Solid State Electronics **17**, 1217 (1974).
- <sup>53</sup>L. J. van der Pauw. *A Method of Measuring the Resistivity and Hall Coefficient on Lamellae of Arbitrary Shape*. Philips Technical Review **20**, 220 (1959).
- <sup>54</sup>Tupta. *Instrumentation and Techniques for Measuring High Resistivity and Hall Voltage of Semiconducting Materials*. Keithley Instruments, Inc. (2005).
- <sup>55</sup>S. Zhang, B. Shang, J. Yang, W. Yan, S. Wei and Y. Xie. *From VO<sub>2</sub>(B) to VO<sub>2</sub>(A) nanobelts: first hydrothermal transformation, spectroscopic study and first principles calculation*. Physical Chemistry Chemical Physics **13**, 3, 15873 (2011).
- <sup>56</sup>A. Chen, Z. Bi, W. Zhang, J. Jian, Q. Jia and H. Wang. *Textured metastable VO<sub>2</sub>(B) thin films on SrTiO<sub>3</sub> substrates with significantly enhanced conductivity*. Applied Physics Letters **104**, 071909 (2014).
- <sup>57</sup>S. Lee, I. Ivanov, J. Keum and H. Lee. *Epitaxial stabilization and phase instability of VO<sub>2</sub> polymorphs*. Scientific Reports **6**, 19621 (2016).
- <sup>58</sup>W. D. Kingery, H. K. Bowen, and D. R. Uhlmann, *Introduction to Ceramics*, 2nd ed. John Wiley and Sons, New York, 1976, p. 595.
- <sup>59</sup>D. Ligny and P. Richet. *High-temperature heat capacity and thermal expansion of SrTiO<sub>3</sub> and SrZrO<sub>3</sub> perovskites*. Physical Review **53**, 3013 (1996).
- <sup>60</sup>S. Corr, M. Grossman, Y. Shi, K. Heier, G. Stucky and R. Seshadri. *VO<sub>2</sub>(B) nanorods: solvothermal preparation, electrical properties, and conversion to rutile VO<sub>2</sub> and V<sub>2</sub>O<sub>3</sub>*. Journal of Materials Chemistry **19**, 4362 (2009).

- <sup>61</sup>D. Fu, K. Liu, T. Tao, K. Lo, C. Cheng, B. Liu, R. Zhang, H. Bechtel and J. Wu. *Comprehensive study of the metal-insulator transition in pulsed laser deposited epitaxial VO<sub>2</sub> thin films*. Journal of Applied Physics **113**, 043707 (2013).
- <sup>62</sup>J. Goodenough. *The Two Components of the Crystallographic Transition in VO<sub>2</sub>*. Journal of Solid State Chemistry **3**, 490 (1971).
- <sup>63</sup>S. Lu, L. Hou and F. Gan. *Structure and Optical Property Changes of Sol-Gel Derived VO<sub>2</sub> Thin Films*. Advance Materials **9**, 244 (1997).
- <sup>64</sup>W. Brückner, W. Moldenhauer, H. Wich, E. Wolf, H. Oppermann, U. Gerlach and W. Reichelt. *The Range of Homogeneity of VO<sub>2</sub> and the Influence of the Composition on the Physical Properties – The Change of the Physical Properties in the Range of Homogeneity*. Physica Status Solidi (a) **29**, 63 (1975).
- <sup>65</sup>C. Griffiths and H. Eastwood. *Influence of stoichiometry on the metalsemiconductor transition in vanadium dioxide*. Journal of Applied Physics **45**, 2201 (1974).
- <sup>66</sup>F. Song and B. White Jr. *Growth of ultra thin vanadium dioxide thin films using magnetron sputtering*. arXiv: 1608.03911, (2016). <https://arxiv.org/abs/1608.03911>
- <sup>67</sup>Q. Wang, J. Pan, M. Li, Y. Luo, L. Zhong and G. Li. *VO<sub>2</sub> (B) Nanosheets as Cathode Material for Li-ion Battery*. Journal of Materials Science and Technology **31**, 630 (2015).
- <sup>68</sup>J. Ni, W. Jiang, K. Yu, Y. Gao and Z. Zhu. *Hydrothermal synthesis of VO<sub>2</sub> (B) nanostructures and application in aqueous Li-ion battery*. Electrochimica Acta **56**, 2122 (2011).
- <sup>69</sup>K. Su, T. Naka, N. Azhan, K. Okimura and M. Higuchi. *Oriented growth of VO<sub>2</sub> (B) thin films on Mo foils by reactive sputtering for lithium ion batteries*. Thin Solid Films **616**, 95 (2016).
- <sup>70</sup>ASTM E1382-97 (2010). *Standard Test Methods for Determining Average Grain Size*. ASTM International, West Conshohocken, PA, 2010, [www.astm.org](http://www.astm.org)
- <sup>71</sup>I. Horcas, F. R. J. M. Gómez-Rodríguez, J. Colchero, J. Gómez-Herrero and A. M. Baro, "WSXM: A software for scanning probe microscopy and a tool for nanotechnology," *Review of Scientific Instruments*, vol. 78, no. 1, 2007.
- <sup>72</sup>J. Seto. *The electrical properties of polycrystalline silicon films*. Journal of Applied Physics **46**, 5247 (2016).